



저작자표시-비영리-변경금지 2.0 대한민국

이용자는 아래의 조건을 따르는 경우에 한하여 자유롭게

- 이 저작물을 복제, 배포, 전송, 전시, 공연 및 방송할 수 있습니다.

다음과 같은 조건을 따라야 합니다:



저작자표시. 귀하는 원저작자를 표시하여야 합니다.



비영리. 귀하는 이 저작물을 영리 목적으로 이용할 수 없습니다.



변경금지. 귀하는 이 저작물을 개작, 변형 또는 가공할 수 없습니다.

- 귀하는, 이 저작물의 재이용이나 배포의 경우, 이 저작물에 적용된 이용허락조건을 명확하게 나타내어야 합니다.
- 저작권자로부터 별도의 허가를 받으면 이러한 조건들은 적용되지 않습니다.

저작권법에 따른 이용자의 권리는 위의 내용에 의하여 영향을 받지 않습니다.

이것은 [이용허락규약\(Legal Code\)](#)을 이해하기 쉽게 요약한 것입니다.

[Disclaimer](#)

공학석사 학위논문

Development of Multiscale
Simulation Framework for
Thermal Protection System
Ablation Analysis

열차폐구조물의 삭마 해석을 위한 멀티스케일
시뮬레이션 환경 구축

2021 년 2 월

서울대학교 대학원

협동과정 우주시스템 전공

박 태 훈

Development of Multiscale Simulation Framework for Thermal Protection System Ablation Analysis

열차폐구조물의 삭마 해석을 위한
멀티스케일 시뮬레이션 환경 구축
지도 교수 윤 군 진

이 논문을 공학석사 학위논문으로 제출함
2020 년 12 월

서울대학교 대학원
협동과정 우주시스템 전공
박 태 훈

박태훈의 공학석사 학위논문을 인준함
2020 년 12 월

위 원 장 _____ 신 상 준 (인)

부위원장 _____ 윤 군 진 (인)

위 원 _____ 이 복 직 (인)



Abstract

Development of Multiscale Simulation Framework for Thermal Protection System Ablation Analysis

PARK Taehoon

Interdisciplinary Program in Space System

The Graduate School

Seoul National University

This thesis aims to independently perform ablation analysis at each nano and macro scale as a preliminary study to perform multiscale ablation analysis of thermal protection systems (TPS). Ablation analysis of carbon/phenolic composites using macro-scale finite element analysis and oxidation analysis of SiC using nanoscale molecular dynamics simulation are performed. Phenomena in ablation of carbon/phenolic composite such as in-depth heat conduction, pyrolysis, gas diffusion, surface heat flux, and recession are implemented in commercial finite element program ABAQUS using

user subroutines written in Fortran. The developed code is compared with the open-source program PATO results for four one-dimensional test cases of various boundary conditions, and the results are well consistent. Naive 2D implementation is also conducted. The oxidation of SiC is analyzed at the nanoscale using molecular dynamics simulation. SiC exhibits complex oxidation properties due to its peculiar lattice structure. Here, the effect of surface orientation and the effect of temperature are analyzed. In the simulation, AOs (atomic oxygen) of 7 km/s collide on a SiC structure under various conditions. The difference in reactivity according to the surface orientation is analyzed through simulation using three surface orientation (100), (110), (111) structures with NVE condition, and the effect of temperature to oxidation is analyzed through simulation under NVT conditions with five different temperatures (600, 900, 1200, 1800, and 2000 K).

Keywords: Thermal protection system, carbon/phenolic composite, silicon carbide, multiscale simulation, molecular dynamics, finite element method

Student Number: 2019-25121

Table of contents

Abstract.....	i
Table of contents	iii
List of figures.....	v
List of tables	viii
1. Introduction.....	1
1.1. Thermal protection system and materials	1
1.2. Research trends in TPS analysis.....	4
1.3. Purpose and contributions of the research.....	7
2. Macro–scale ablation analysis of carbon/phenolic composite using the finite element method.....	10
2.1. Physical description of carbon/phenolic composite ablation	10
2.1.1. In–depth heat transfer	12
2.1.2. Material decomposition.....	12
2.1.3. In–depth gas diffusion.....	13
2.1.4. Surface heat flux boundary condition.....	15
2.1.5. Theoretical ablative composite for open testing (TACOT)	18
2.2. ABAQUS implementation	19
2.2.1. Dual–domain system.....	19
2.2.2. Analysis procedure and ABAQUS user subroutines.	22
3. Nanoscale oxidation analysis of SiC ceramic using	

molecular dynamics simulation	34
3.1. Silicon Carbide (SiC) and Atomic Oxygen (AO).....	34
3.2. Molecular dynamics.....	35
3.3. Reaxff: The Reactive Force–Field.....	37
3.4. Simulation Procedure	40
3.4.1. SiC structure modeling	40
3.4.2. Oxidation simulation	45
4. Results and discussion.....	48
4.1. Verification of macro–scale ablation analysis of carbon/phenolic composite	48
4.1.1. Case 1: Constant temperature, no recession	52
4.1.2. Case 2: Low heating, no recession	54
4.1.3. Case 3: Low heating, recession	57
4.1.4. Case 4: High heating, recession.....	59
4.1.5. Case 5: High heating, recession in 2D.....	61
4.2. Nanoscale oxidation analysis of SiC ceramic.....	65
4.2.1. Effect of surface orientation	65
4.2.2. Effect of temperature	70
5. Conclusions and future works	76
5.1. Conclusions.....	76
5.2. Future works	77
국문초록.....	91

List of figures

FIGURE 1 (A) SEEN FROM THE INTERNATIONAL SPACE STATION, THE SOYUZ TMA-05M DESCENT MODULE BEGINS TO RE-ENTER THE EARTH'S ATMOSPHERE. FROM [2]. CREDIT: NASA. (B) BLOCKS OF ABLATIVE MATERIAL TO THE THERMAL PROTECTION SYSTEM FOR THE ORION SPACECRAFT. FROM [3]. CREDIT: <i>NASA/ISAAC WATSON</i>	1
FIGURE 2 SCHEMATIC OF MULTISCALE SIMULATION FRAMEWORK FROM ATOMIC TO SYSTEM SCALE	9
FIGURE 3 VARIOUS PHENOMENA OCCURRING DURING ABLATION.	10
FIGURE 4 SURFACE ENERGY BALANCE.	15
FIGURE 5 (A) SCHEMATIC OF THE DUAL-DOMAIN SYSTEM AND (B) THE ABAQUS VISUALIZATION OF THE DUAL-DOMAIN SYSTEM.	21
FIGURE 6 PROCEDURE FOR ABLATION ANALYSIS OF CARBON/PHENOLIC COMPOSITES USING ABAQUS.....	22
FIGURE 7 TYPICAL GRAPH OF INTERATOMIC LENNARD-JONES POTENTIAL	37
FIGURE 8 INTERATOMIC DISTANCE DEPENDENCY OF THE CARBON—CARBON BOND ORDER. REPRINTED WITH PERMISSION FROM [37]. COPYRIGHT (2001) AMERICAN CHEMICAL SOCIETY.	39
FIGURE 9 PROCEDURE OF SiC OXIDATION SIMULATION	40
FIGURE 10 3C-SiC CRYSTAL STRUCTURE.....	41
FIGURE 11 (A) BULK 3C-SiC STRUCTURE AND TOP VIEWS OF THREE DIFFERENT SURFACE ORIENTATIONS: (100) (A), (110) (B), AND (111) (C). ADAPTED WITH PERMISSION FROM [38]. COPYRIGHT (2020) AMERICAN INSTITUTE OF AERONAUTICS AND ASTRONAUTICS.	42
FIGURE 12 PREPROCESSED INITIAL STRUCTURES WITH DIFFERENT SURFACE ORIENTATIONS. ADAPTED WITH PERMISSION FROM [38]. COPYRIGHT (2020) AMERICAN INSTITUTE OF AERONAUTICS AND ASTRONAUTICS.....	44
FIGURE 13 OVERALL CONFIGURATION OF THE SIMULATION BOX. ADAPTED WITH PERMISSION FROM [38]. COPYRIGHT (2020) AMERICAN INSTITUTE OF AERONAUTICS AND ASTRONAUTICS.....	47
FIGURE 14 GEOMETRY AND BOUNDARY CONDITIONS OF THE ANALYSIS MODEL.....	51
FIGURE 15 (A) TEMPERATURE, (B) PRESSURE, AND (C) DENSITY OF CASE 1 AT 60 SEC	51

FIGURE 16 CASE 1: TEMPERATURE PROFILE (VS. PATO).....	53
FIGURE 17 CASE 1: BLOWING RATES, PYROLYSIS ZONE, AND RECESSION (VS. PATO).....	54
FIGURE 18 HEAT FLUX BOUNDARY CONDITION PROFILE FOR CASE 2-4.....	55
FIGURE 19 CASE 2: TEMPERATURE PROFILE (VS. PATO).....	56
FIGURE 20 CASE 2: BLOWING RATES, PYROLYSIS ZONE, AND RECESSION	57
FIGURE 21 CASE 3: TEMPERATURE PROFILE (VS. PATO).....	58
FIGURE 22 CASE 3: BLOWING RATES, PYROLYSIS ZONE, AND RECESSION	59
FIGURE 23 CASE 4: TEMPERATURE PROFILE (VS. PATO).....	60
FIGURE 24 CASE 4: BLOWING RATES, PYROLYSIS ZONE, AND RECESSION	61
FIGURE 25 GEOMETRY OF 2D MODEL.....	63
FIGURE 26 (A) TEMPERATURE, (B) DENSITY, AND (C) PRESSURE OF CASE 5 AT 40 SEC	64
FIGURE 27 TEMPERATURE PROFILE (VS. ABLATION WORKSHOP[60])	65
FIGURE 28 STRUCTURAL CHANGES OF (A) (100), (B) (110), AND (C) (111) SiC AFTER AO COLLISION. ADAPTED WITH PERMISSION FROM [38]. COPYRIGHT (2020) AMERICAN INSTITUTE OF AERONAUTICS AND ASTRONAUTICS.....	67
FIGURE 29 PRODUCTS FORMED DUE TO AO COLLISION: A) AMORPHOUS SiO _x , AND (B) CO(g). ADAPTED WITH PERMISSION FROM [38]. COPYRIGHT (2020) AMERICAN INSTITUTE OF AERONAUTICS AND ASTRONAUTICS.....	68
FIGURE 30 SURFACE CARBON BONDING STRUCTURES. ADAPTED WITH PERMISSION FROM [38]. COPYRIGHT (2020) AMERICAN INSTITUTE OF AERONAUTICS AND ASTRONAUTICS.	68
FIGURE 31 MASS PROFILES (A) FROM 0 TO 40PS AND (B) 0 TO 25 PS. ADAPTED WITH PERMISSION FROM [38]. COPYRIGHT (2020) AMERICAN INSTITUTE OF AERONAUTICS AND ASTRONAUTICS.....	69
FIGURE 32 NORMALIZED MASS AND TEMPERATURE PROFILE OF (100) SiC STRUCTURE (A) OVER THE ENTIRE SIMULATION TIME, AND (B) IN THE OXIDATION REGION. ADAPTED WITH PERMISSION FROM [38]. COPYRIGHT (2020) AMERICAN INSTITUTE OF AERONAUTICS AND ASTRONAUTICS.....	74
FIGURE 33 NORMALIZED MASS AND NUMBER OF CO MOLECULES IN THE OXIDATION. ADAPTED WITH PERMISSION FROM [38]. COPYRIGHT (2020) AMERICAN INSTITUTE OF AERONAUTICS AND ASTRONAUTICS.....	75
FIGURE 34 NORMALIZED MASS OF SiC DURING INITIAL AO COLLISION (0-10PS) AT VARIOUS	

TEMPERATURES. ADAPTED WITH PERMISSION FROM [38]. COPYRIGHT (2020) AMERICAN
INSTITUTE OF AERONAUTICS AND ASTRONAUTICS..... 75

List of tables

TABLE 1 SIMULATION BOX SIZE AND NUMBER OF ATOMS FOR EACH ORIENTATION.....	45
TABLE 2 SUMMARY OF SIMULATION CASES.....	48
TABLE 3 SUMMARY OF TEST CASE.....	50
TABLE 4 BOUNDARY CONDITION OF CASE 1	53
TABLE 5 BOUNDARY CONDITION OF CASE 2 AND CASE3.....	56
TABLE 6 BOUNDARY CONDITION OF CASE 4	60
TABLE 7 HEAT FLUX DISTRIBUTION DEPENDING ON COORDINATE [60].....	63
TABLE 8 BOUNDARY CONDITION OF CASE 5	64

1. Introduction

1.1. Thermal protection system and materials

A phenomenon called aerodynamic heating occurs in a vehicle that passes through the atmosphere at high speed. Air is condensed at the surface and generates heat (Figure 1 (a)). This heat increases the vehicle's surface temperature to nearly 3000K at a typical reentry condition where maximum speed is almost Mach 25 [1]. A thermal protection system (TPS) is used to protect the aircraft from such high temperatures. The TPS has been used in various vehicles, from space vehicles such as space shuttles and reentry capsules to missiles (Figure 1 (b)).

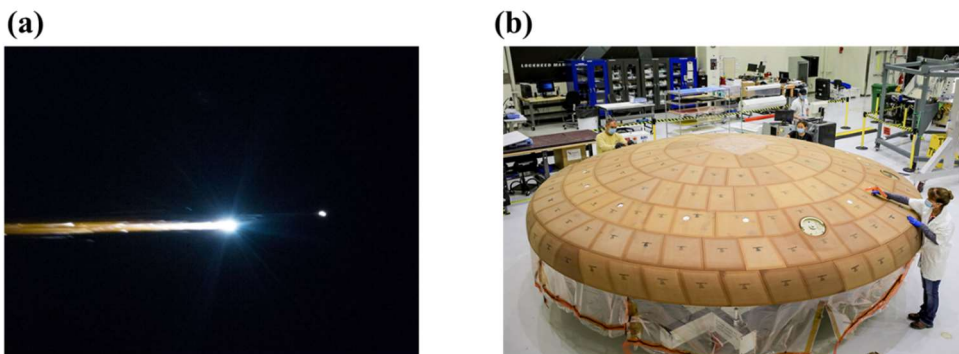


Figure 1 (a) Seen from the International Space Station, the Soyuz TMA-05M descent module begins to re-enter the Earth's

atmosphere. From [2]. Credit: NASA. (b) Blocks of ablative material to the thermal protection system for the Orion spacecraft. From [3]. Credit: *NASA/Isaac Watson*

The mission environment of the TPS varies depending on the vehicle's objective. Suitable TPS material must be selected for a successful mission. TPS materials are primarily divided into two: ablative and non-ablative [4].

Ablative TPS is mainly made of polymeric materials such as phenol. It is generally made in a composite material containing fibers such as carbon in a polymer matrix. PICA (Phenolic Integrated Carbon Ablator), a carbon/phenolic composite developed by NASA, is representative [4,5]. PICA was used as a TPS material for Mars Science Laboratory (MSL), a vehicle used to land the Curiosity rover on Mars in 2012 [6]. Another example of ablative TPS material is AVCOAT used for the TPS on NASA's Apollo command module and Orion crew module [7]. AVCOAT is composed of phenol resin and a fiberglass honeycomb structure [8].

Polymeric materials decompose when exposed to a high-temperature environment, which is called pyrolysis. The gas generated by pyrolysis flows to the surface of the TPS and blocks

the heat load. The pyrolyzed polymer turns into a char layer. Char layer is composed of carbon atoms, so it has a very high reactivity to oxygen atoms in the atmosphere. Surface erosion occurs not only by oxidation by atomic oxygen but also by various mechanical and chemical reactions such as sublimation and melting. Ablative TPS is difficult to reuse because it suffers serious damage once used, but has an advantage that it can be used in harsher environments than non-ablative TPS [4].

On the other hand, unlike ablative TPS that blocks heat load by inducing material damage, non-ablative TPS uses re-radiation for insulation [4]. Non-ablative TPS suppresses damage as much as possible. In general, heat shielding performance is lower than that of ablative TPS. However, it has the advantage of reusability, so it has been actively developed in recent years. Ultra high-temperature ceramics (UHTC) is one of the representative non-ablative TPS materials. In general, UHTC is a binary compound in which B, C, and N are combined with transition metals such as Zr, Hf, Ti, Nb, and Ta [9,10]. UHTC has high hardness, stiffness, and melting temperature owing to strong covalent bonds between transition metals and B, C,

or N. Therefore, it can withstand extreme temperature, heat fluxes, mechanical loads, chemical reactions, and other conditions that it can encounter with during mission [9,11]. Research has also been conducted to increase oxidation resistance through additives such as SiC [10,12–15].

1.2. Research trends in TPS analysis

Regardless of ablative or non-ablative characteristics, the damage will occur in extreme environments. Predicting the damage and considering it in the design is essential for the stability of the vehicle. Many macro-scale models had been developed since the 1960s. Mathematical models of physical phenomena such as in-depth material response, laminar boundary layer, and transport properties were preceded [16–21], and the Charring Material Ablation code (CMA) was developed based on them [22]. Fully Implicit Ablation and Thermal (FIAT) code was developed, which implemented a fully implicit scheme to CMA's theory for numerical stability [23]. Since the CMA/FIAT code was limited to one-dimension (1D), it was expanded to two and three -dimensions(2D, 3D), and TITAN [24] and 3dFIAT [25] were developed, respectively [26]. Models based

on the CMA theory assume simplified gas diffusion. The pyrolysis gas is assumed in thermal equilibrium with the solid material, the residence time inside the solid is negligibly short, and the gas exits vertically to the surface [17]. These assumptions were not suitable for more than 2D cases, and efforts were made to resolve them. Porous material Analysis Toolbox based on OpenFOAM (PATO) code implemented Darcy's law to simulate the movement of gas flowing through porous materials [27]. The numerical analysis scheme is different depending on the analysis code. CMA used the finite difference method, FIAT and PATO used the finite volume method for numerical analysis. The finite element method has gained more attention in recent years owing to its improved computational power, flexibility, and applicability to complex shapes compared to the finite difference or volume method [26,28–31]. Charring Ablator Response (CHAR) [32] and Heat Transfer and Erosion Analysis (HERO) [33] code are representative tools using the finite element method. These codes lack expandability as they are developed in in-house codes. Therefore, research to perform ablation analysis using a commercial finite element analysis program such as ABAQUS is

ongoing. Wang et al. implemented CMA/FIAT-based ablation model using various user subroutines [26,34].

Recently, a method of adding a nanoscale approach using Molecular Dynamics (MD) simulation has emerged to overcome the limitations of macroscopic numerical analysis. The MD simulation is a technique that calculates the motion of atoms through the calculation of potential energy between atoms. The interatomic potential is obtained through ab-initio calculation, and the collection of potential information between different elements calculated by the ab-initio is called a force field. Force fields such as Polymer Consistent Force Field (PCFF) [35] and Condensed-phase Optimized Molecular Potentials for Atomistic Simulation Studies (COMPASS) [36] are developed and continuously updating. Although many studies have been conducted using these force fields, these classical force fields have the disadvantage that they cannot simulate the formation and destruction of chemical bonds. The reactive force field (ReaxFF) [37] was developed to overcome this limitation. The ReaxFF can simulate chemical reactions because it not only predicts the position of each atom using interatomic potential but also calculates the bond order

using the distance between atoms. The ReaxFF has been applied to study heat shield materials, such as simulating the collision of the most unstable oxygen atoms in the reentry environment [38–46] or analyzing the pyrolysis of the polymer [47–50].

1.3. Purpose and contributions of the research

Molecular dynamics simulation can provide insight into various physical, chemical reactions at the nanoscale that are difficult to observe at the macro scale. However, a large gap in time and length scale between nano and macro-scale is the limit. It is essential to develop a multiscale approach to overcome the large discrepancy between scales (Figure 2). There have been many efforts to use the analysis results in molecular dynamics to the macroscale finite element analysis [51–55]. Mainly, the material properties were measured using molecular dynamics, and they were used for macro scale analysis. Mechanical properties such as stress–strain relationship [56], transport properties such as diffusivity [54], and thermal properties such as heat conductivity [55] and also pyrolysis properties for TPS [48] were studied. Before scale bridging, a solid understanding of the analysis methods and results at each scale is

required. Therefore, as a preliminary research for multiscale analysis, the macro-scale and nanoscale analysis is individually conducted in this thesis. A code for ablation analysis of carbon/phenolic composites at a macro-scale is developed using finite element program ABAQUS [57]. ABAQUS is suitable for performing complex ablation analysis because user can implement the user-defined material model and boundary conditions through various Fortran subroutines. In addition, it has the advantage of being able to use convenient tools provided by commercial programs such as an accurate finite element solver and powerful visualization. Oxidation analysis of SiC is performed using molecular dynamics with LAMMPS [58] which is an open source program that can perform large scale molecular dynamics simulations developed by Sandia National Laboratories. We hope that these analysis results at each scale will ultimately serve as a platform for developing a scale bridging method for multiscale analysis.

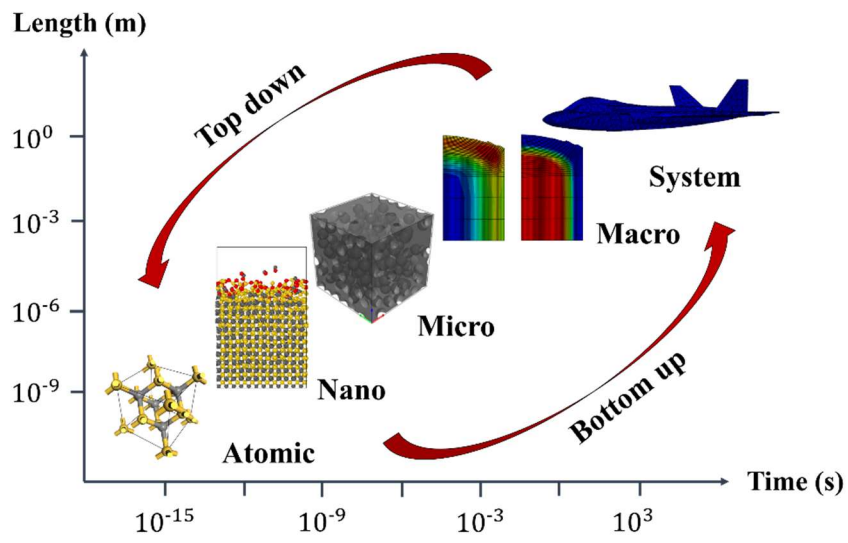


Figure 2 Schematic of multiscale simulation framework from atomic to system scale

2. Macro-scale ablation analysis of carbon/phenolic composite using the finite element method

2.1. Physical description of carbon/phenolic composite ablation

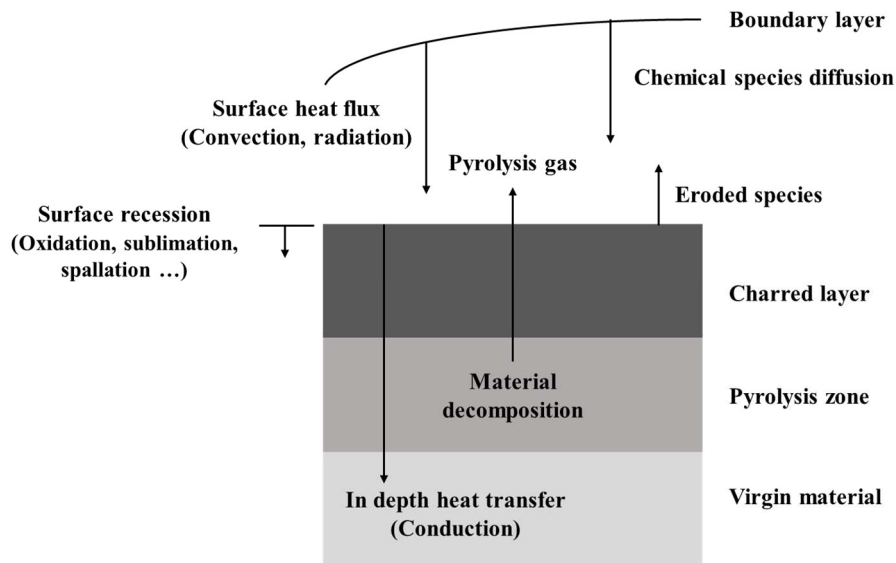


Figure 3 Various phenomena occurring during ablation.

In the aerodynamic heating situation, the ablative thermal protection system material experiences the phenomena shown in Figure 3. The heat generated by aerodynamic heating is transferred to the thermal protection system in convection or radiation. When this heat encounters the material, it is transferred into the material in the form of conduction. The transferred heat raises the temperature of

the material. When the temperature rises, pyrolysis of the polymer material occurs. Phenol in a solid-state releases pyrolysis gases and turns into a charred layer composed of carbon. This process is endothermic and absorbs the heat. Besides, the generated gas escapes out of the material and transfers energy, so it releases heat load. Material properties change as it changes from a virgin polymer composite to a charred layer. The charred layer is created from the surface and gradually propagates downward. The charred surface layer is damaged by various physical and chemical reactions, which cause shape change. The most significant contributor to this erosion is collisions with highly reactive species, mostly oxygen atoms. Besides, melting and sublimation due to high temperature and spallation due to friction occur.

To model the ablation phenomenon of the thermal protection system, it is necessary to solve these various phenomena numerically. The mathematical derivation of each phenomenon can be confirmed in various papers [16–21,28,29]. Next, the equation for each phenomenon, and the meaning of the equation will be described.

2.1.1. In-depth heat transfer

The equation representing in-depth heat transfer is as follows.

$$\rho C_p \frac{\partial T}{\partial t} = \nabla \cdot (k \nabla T) + (h_g - \bar{h}) \frac{\partial \rho}{\partial t} + \dot{s} \rho C_p \nabla T + \dot{m}_g'' C_{pg} \nabla T \quad (1)$$

ρ is the density of the material, C_p is the specific heat, k is the thermal conductivity, h_g is the enthalpy of the pyrolysis gas, \bar{h} is the average enthalpy between virgin and charred material, \dot{s} is the speed of surface recession, and \dot{m}_g'' is the mass flux of the pyrolysis gas. The left term of the equal sign is the internal energy of the solid material. The first term on the right of the equal sign is the energy transferred by conduction expressed in Fourier's law, the second term is energy consumption due to pyrolysis, the third term is the energy term associated with surface erosion, and the last term is the energy due to the diffusion of pyrolysis gas.

2.1.2. Material decomposition



Phenol is pyrolyzed in a high-temperature environment. As can be seen in Eq. (2), virgin material decomposes into char consisting of

carbon and generate pyrolysis gas consisting of C, H, O, etc. The generated pyrolysis gas exits the material and reduces its density. As it changes from virgin material to char, the density and the density and various physical properties change. Therefore, the pyrolysis process must be accurately predicted to obtain the properties. According to Goldstein [59], the density change due to pyrolysis takes Arrhenius equation form as follows

$$\frac{\partial \rho}{\partial t} = -A \exp\left(-\frac{E}{RT}\right) \rho_v \left(\frac{\rho - \rho_c}{\rho_v}\right)^\psi \quad (3)$$

A is the pre-exponential factor, E is the activation energy, R is gas constant, T is temperature, ρ is current density, ρ_c is char density, ρ_v is the virgin material density, and ψ is reaction order.

2.1.3. In-depth gas diffusion

When a polymer composite material is pyrolyzed, gas is produced. This gas moves through the porous material and forms a gas flux. Some assumptions are needed to simulate the movement of gas. The pyrolysis gas generated first is in equilibrium with the solid material. Second, the time for gas to existing inside the solid is short. With these assumptions, Eq. (4) is derived, which means pyrolysis gas

generation is equal to the decomposition of virgin material. The time derivative of density change can be expressed as follows [28].

$$\nabla \cdot \dot{m}_g'' = \frac{\partial \rho}{\partial t} \quad (4)$$

Generated gas flows through the porous material and Darcy's law expresses the motion of a fluid through a porous material. Darcy's law is written as follows,

$$\mathbf{q} = \frac{\kappa}{\mu} \nabla P \quad (5)$$

\mathbf{q} is the instantaneous flux, κ is the permeability, μ is the fluid's dynamic viscosity, and P is the pressure.

Fluid velocity travel through a porous medium is determined by flux (\mathbf{q}), and porosity (ϕ) as Eq. (6).

$$\mathbf{u} = \frac{\mathbf{q}}{\phi} \quad (6)$$

Mass flux of pyrolysis gas is expressed as follows.

$$\dot{m}_g'' = \rho_g \mathbf{u} \quad (7)$$

Combining Eq. (6) and Eq. (7) yields Eq. (8).

$$\dot{m}_g'' = -\frac{\rho_g \kappa}{\mu \phi} \nabla P \quad (8)$$

The final form of pyrolysis gas diffusion in a porous medium can be

expressed as Eq. ((9)) using Eq. (4) and Eq. (8).

$$\frac{\partial \rho}{\partial t} + \nabla \cdot \left(\frac{\rho g \kappa}{\mu \phi} \nabla P \right) = 0 \quad (9)$$

2.1.4. Surface heat flux boundary condition

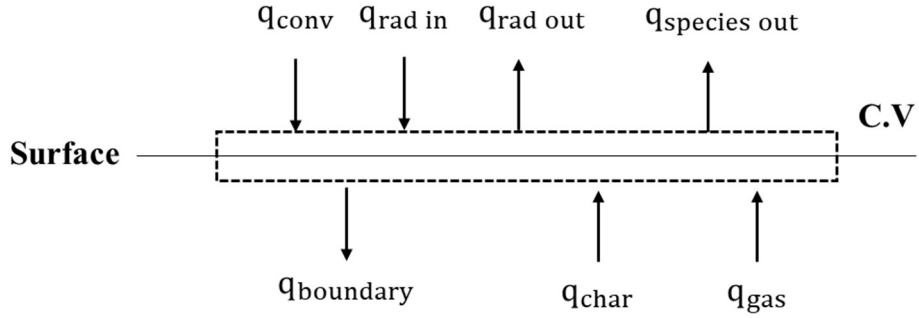


Figure 4 Surface energy balance.

Figure 4 shows various types of energy enter and exit the control volume adjacent to the TPS surface, and the total sum of energy entry and exit is zero according to the energy conservation law. Surface heat flux as boundary conditions can be obtained through this relationship.

Energy entering the control volume is the convective heat flux (q_{conv}), the radiative heat flux ($q_{rad in}$), the energy of pyrolysis gas entering the surface (q_{gas}) and the energy by char consumption (q_{char}).

Energy exiting the control volume is the radiative heat flux ($q_{rad out}$),

the energy of species blowing outside ($q_{\text{species out}}$), and the heat flux transferred to a material in the form of conduction (q_{boundary}).

Using the law of conservation of energy (Eq. (10)), Eq. (11) can be obtained.

$$E_{in} = E_{out} \quad (10)$$

$$\begin{aligned} q_{\text{conv}} + q_{\text{rad in}} + q_{\text{gas}} + q_{\text{char}} \\ = q_{\text{rad out}} + q_{\text{species out}} + q_{\text{boundary}} \end{aligned} \quad (11)$$

Diffusive heat flux coming from the boundary layer is expressed as Eq. (12). $\rho_e U_e C_H$ is the convection heat transfer coefficient. ρ_e and U_e denote the density and velocity of flow at the edge of the boundary layer, respectively. h_r is the recovery enthalpy, h_w is the enthalpy on the surface.

$$q_{\text{conv}} = \rho_e U_e C_H (h_r - h_w) \quad (12)$$

According to the Stefan–Boltzmann law, net radiative heat flux considering both incoming and outgoing radiative heat flux is Eq. (13). σ is Stefan–Boltzmann constant and ε is emissivity.

$$q_{\text{rad}} = q_{\text{rad in}} - q_{\text{rad out}} = -\sigma\varepsilon(T_w^4 - T_\infty^4) \quad (13)$$

Energy, associated with material flux, can be calculated with mass

transfer coefficient ($\rho_e U_e C_M$), mass flux (\dot{m}''), and enthalpy (h). q_{gas} , q_{char} , and $q_{species\ out}$ are as follows.

$$q_{gas} = \dot{m}_g'' \cdot h_g \quad (14)$$

$$q_{char} = \dot{m}_c'' \cdot h_c \quad (15)$$

$$q_{species\ out} = (\rho u)_w \cdot h_w \quad (16)$$

The species flux leaving the surface can be obtained as the sum of the pyrolysis gas flux and the char flux as Eq 17.

$$(\rho u)_w = \dot{m}_g'' + \dot{m}_c'' \quad (17)$$

These mass fluxes can be expressed as non-dimensional ablation rates by dividing mass transfer coefficients as follows [28].

$$B' = \frac{(\rho u)_w}{\rho_e U_e C_M}, \quad B_g' = \frac{\dot{m}_g''}{\rho_e U_e C_M}, \quad B_c' = \frac{\dot{m}_c''}{\rho_e U_e C_M} \quad (18)$$

Assume that the Lewis number and Prandtl number are unity ($C_M = C_H$) [28].

Combining Eq. (11)–Eq. (18), the final form of surface heat flux in boundary condition is obtained as follows.

$$\begin{aligned}
q_{boundary} = & \rho_e U_e C_H (\dot{h}_r - \dot{h}_w) \\
& + \rho_e U_e C_H (B'_c \dot{h}_c + B'_g \dot{h}_g - B'_w \dot{h}_w) \\
& - \sigma \varepsilon (T_w^4 - T_\infty^4)
\end{aligned} \tag{19}$$

2.1.5. Theoretical ablative composite for open testing (TACOT)

For accurate ablation analysis, not only accurate formulas but also accurate material properties are important. In this study, the material properties are taken from the TACOT database [60]. TACOT provides thermochemical properties of low-density carbon/phenolic ablator as a free open database for ablation analysis code verification. Structural properties (volume fraction, porosity, permeability, etc.), thermal properties (heat capacity, thermal conductivity, and enthalpy that depend on the temperature), constants for decomposition kinetics, pyrolysis gas properties (molar mass, heat capacity, enthalpy, viscosity, density, etc.) and B' table for heat flux boundary conditions is included in TACOT.

2.2. ABAQUS implementation

2.2.1. Dual-domain system

Both the heat transfer equation and the gas diffusion equation have similar forms involving Laplacian and time derivatives. ABAQUS UMATHT is a subroutine for solving the heat transfer equation, but the gas diffusion equation can also be solved using the governing equation's similarity. The key idea is to consider pressure at an imaginary temperature. If gas diffusion properties such as viscosity and permeability are used instead of heat transfer properties such as thermal conductivity and heat capacity and apply initial and boundary conditions of pressure value instead of initial and boundary conditions of temperature value, ABAQUS solves the gas diffusion equation rather than heat transfer equation. To perform both heat transfer analysis and gas diffusion analysis simultaneously, one more domain is required in addition to the original analysis domain. Two domains are identical material, but in ABAQUS, one domain is used for heat transfer analysis and the other for gas diffusion analysis. Data needed for analysis is shared using a common block.

Figure 5(a) is the graphical summary of the dual-domain system. To build a dual-domain system, two parts with the same geometry must be made at first. Two material models are defined and assigned to each part, so the two parts are recognized as different materials, and different material properties can be applied. Then assemble the two parts, as can be seen in Figure 5(b). Heat flux, temperature, and pressure boundary conditions are applied to the appropriate domain. After specifying the analysis parameters, such as the time step, the preprocessed dual-domain system is completed. Several studies have performed simulations by applying this dual-domain system [61–63].

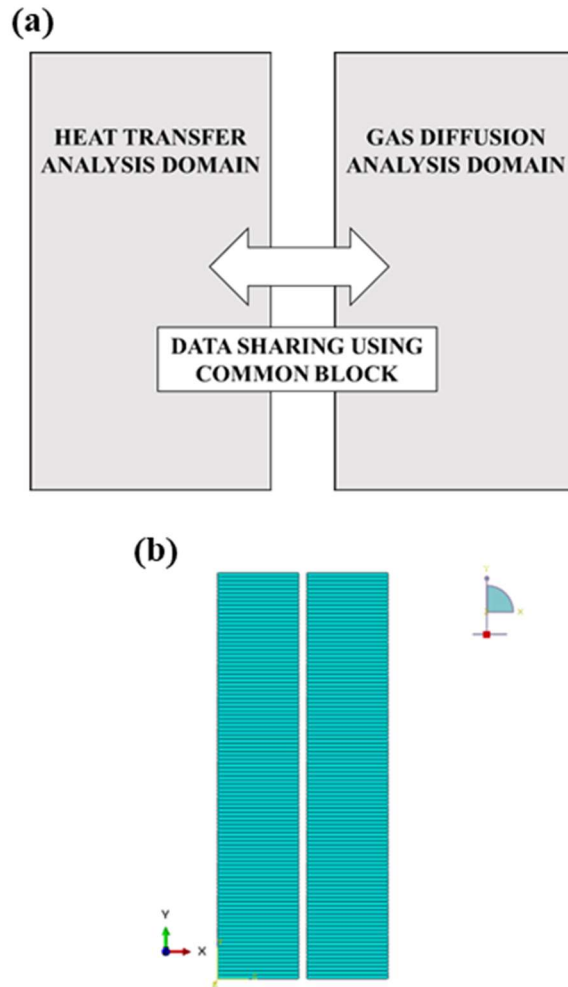


Figure 5 (a) Schematic of the dual-domain system and (b) the ABAQUS visualization of the dual-domain system.

2.2.2. Analysis procedure and ABAQUS user subroutines

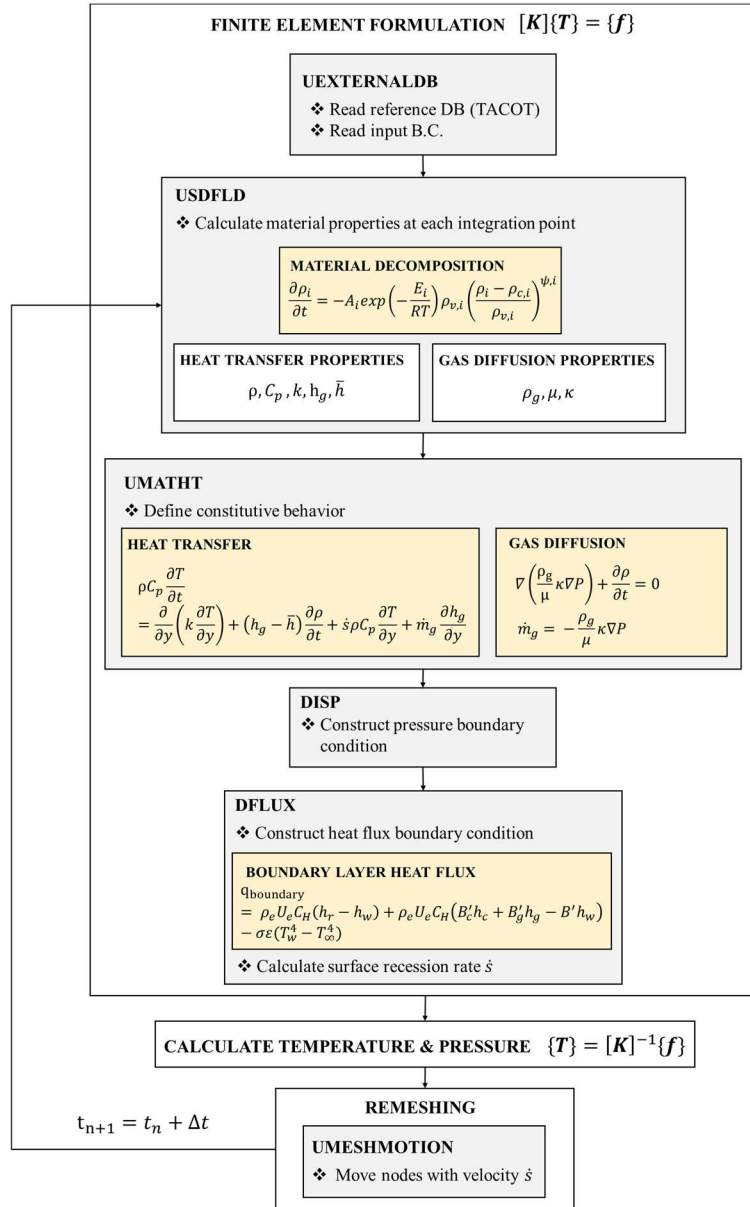


Figure 6 Procedure for ablation analysis of carbon/phenolic composites using ABAQUS.

ABAQUS can modify the governing equation through user subroutines. The equations discussed above are applied to the preprocessed model through various user subroutines. The analysis procedure and the subroutines used are in Figure 6. A detailed description of each subroutine can be found through the ABAQUS user manual [57].

-UEXTERNALDB

UEXTERNALDB is used to open external files and called once at the beginning of the analysis, at the beginning of every increment, at the end of each increment, etc., depending on the needs of the user. Since opening an external file takes a lot of computation time, the files for input or output is opened through UEXTERNALDB at the beginning of the analysis. Then, information necessary for analysis such as information on heat flux distribution according to location, material properties according to the temperature of virgin material, charred material and gas, and B table is read and stored in the COMMON BLOCK.

-USDFLD

USDFLD is called at every integration point and plays a role in

calculating the material properties for heat transfer equation (Eq. (1)) such as density, heat capacity, thermal conductivity, and enthalpy, and the properties for gas diffusion equation (Eq. (9)) such as viscosity, porosity, and permeability. Calculated material properties are stored in COMMON BLOCK and transmitted to other SUBROUTINEs such as UMATHHT.

One of the critical equations, the material decomposition calculation, is solved in USDFLD to calculate material properties. Since $\partial \rho / \partial t$ is a function of temperature and density, as shown in Eq. (3), the temperature and density at the previous increment are required. The density at the previous increment is obtained through the value stored in the COMMON BLOCK, and the temperature at the previous increment is obtained through the GETVRM function. The density is explicitly calculated using the forward finite difference with the following $\partial \rho / \partial t$ values.

$$\rho_t = \rho_{t-\Delta t} + \Delta t \times \left(-A \exp\left(-\frac{E}{RT_{t-\Delta t}}\right) \rho_v \left(\frac{\rho_{t-\Delta t} - \rho_c}{\rho_v}\right)^\psi \right) \quad (20)$$

In the TACOT, since it is composed of three different materials, the total density is calculated using the rule of mixture after calculating the density for each material. I is the volume fraction of

composite material.

$$\rho = \Gamma(\rho_A + \rho_B) + (1 - \Gamma)\rho_C \quad (21)$$

When the density is calculated, the degree of decomposition τ of the material at the current integration point is obtained.

$$\tau = \frac{1 - \frac{\rho_c}{\rho}}{1 - \frac{\rho_c}{\rho_v}} \quad (22)$$

In the case of virgin material that has not undergone pyrolysis, τ is 1, and in the case of wholly pyrolyzed char, τ is 0. Using the τ value, the properties of the material undergoing pyrolysis are obtained as follows. Each virgin material's physical properties and charred material change with temperature, which should also be considered. TACOT DB is used for properties according to temperature.

$$C_p = \tau C_{p,v} + (1 - \tau)C_{p,c} \quad (23)$$

$$k = \tau k_v + (1 - \tau)k_c \quad (24)$$

$$\kappa = \tau \kappa_v + (1 - \tau)\kappa_c \quad (25)$$

The mass-weighted average enthalpy of virgin and char material is calculated as follows.

$$\bar{h} = \frac{\rho_V h_V - \rho_C h_C}{\rho_V - \rho_C} \quad (26)$$

In addition to the solid materials' physical properties, the pyrolysis gas' properties such as the density (ρ_g), the enthalpy (h_g), the heat capacity (C_{pg}), the viscosity (μ) for the pyrolysis gas are also obtained.

All properties are temperature-dependent, so interpolation must be performed to calculate the properties at a specific temperature accurately.

-UMATHT

UMATHT is a subroutine for defining thermal constitutive behavior such as heat transfer and heat generation. The primary energy balance equation in ABAQUS is as follows [57].

$$\int_V \rho \dot{U} dV = \int_S q dS + \int_V r dV \quad (27)$$

V is the volume with surface area S , ρ is the density, \dot{U} is the time rate of internal thermal energy of the material, q is the heat flux per unit area, and r is the external heat into the material per unit volume. q can be rewritten using the heat flux vector \mathbf{f} , and the unit surface normal vector \mathbf{n} .

$$\mathbf{q} = -\mathbf{f} \cdot \mathbf{n} \quad (28)$$

Applying Fourier's law, the equation is rearranged as follows.

Substituting Eq. (28) into Eq. (27) and applying the divergence theorem yields the following relationship.

$$\int_V \rho \dot{U} dV = \int_V \nabla \cdot \vec{f} dV + \int_r r dV \quad (29)$$

Conversion Eq. (29) to weak form for finite element analysis is as follows.

$$\int_V \delta T \rho \dot{U} dV - \int_V \delta \mathbf{g} \cdot \mathbf{f} dV = \int_V \delta T r dV + \int_S \delta T dS \quad (30)$$

\mathbf{g} is the temperature gradient (∇T), and δT is the virtual temperature.

As \dot{U} is the time derivative, backward difference algorithm is used.

$$\dot{U}_{t+\Delta t} = \frac{U_{t+\Delta t} - U_t}{\Delta t} \quad (31)$$

The weak form of the energy balance equation now turns into

$$\begin{aligned} \frac{1}{\Delta t} \int_V \delta T \rho (U_{t+\Delta t} - U_t) dV \\ = \int_V \delta \mathbf{g} \cdot \mathbf{f} dV + \int_V \delta T r dV + \int_S \delta T q dS \end{aligned} \quad (32)$$

The Newton method is used to solve this non-linear system.

Jacobian of Eq. (32) is expressed as

$$\begin{aligned}
\mathbf{J} &= \frac{1}{\Delta t} \int_V \delta T \rho \frac{\partial U}{\partial T} dT dV + \frac{1}{\Delta t} \int_V \delta T \rho \frac{\partial U}{\partial \mathbf{g}} \cdot d\mathbf{g} dV & (33) \\
&- \int_V \delta \mathbf{g} \cdot \frac{\partial \mathbf{f}}{\partial T} dT dV - \int_V \delta \mathbf{g} \cdot \frac{\partial \mathbf{f}}{\partial \mathbf{g}} \cdot d\mathbf{g} dV - \int_V \delta T \frac{\partial r}{\partial T} dT dV \\
&- \int_s \delta T \frac{\partial q}{\partial T} dT dS
\end{aligned}$$

To calculate the Jacobian, six variables must be defined. Three of them are the internal thermal energy per unit mass at the end of the increment (U), the variation of internal thermal energy per unit mass with respect to temperature ($\partial U / \partial T$), and the variation of internal thermal energy per unit mass with respect to the spatial gradients of temperature ($\partial U / \partial \mathbf{g}$). The remaining three are the heat flux related variables, which are the heat flux vector (\mathbf{f}), the variation of heat flux vector with respect to temperature ($\partial \mathbf{f} / \partial T$), and the variation of the heat flux vector with respect to the spatial gradients of temperature ($\partial \mathbf{f} / \partial \mathbf{g}$). Variation of thermal constitutive behavior can be specified by modifying these six variables.

This study aims to establish two domains, heat transfer analysis in one domain and gas diffusion analysis in the other domain. Therefore, the variables of each domain must be defined differently.

In the case of heat transfer analysis, the governing equation is Eq.

(1). It can be divided into two parts (\dot{U}, \mathbf{f}) to relate with Eq. (29).

$$\dot{U} = \rho C_p \frac{\partial T}{\partial t} - \left(\dot{h}_g - \bar{h} \right) \frac{\partial \rho}{\partial t} - \dot{s} \rho C_p \nabla T - \dot{m}_g'' C_{pg} \nabla T \quad (34)$$

$$\mathbf{f} = -k \nabla T \quad (35)$$

Eq. (34) can be changed into incremental form as

$$\begin{aligned} \Delta U = & \rho C_p \Delta T - \left(\dot{h}_g - \bar{h} \right) \Delta \rho - \dot{s} \rho C_p \nabla T \Delta t \\ & - \dot{m}_g'' C_{pg} \nabla T \Delta t \end{aligned} \quad (36)$$

Using Eq. (36), the internal thermal energy per unit mass at the end of the increment (U) is defined as

$$U(t + \Delta T) = U(t) + \Delta U \quad (37)$$

And the variation of internal thermal energy per unit mass with respect to temperature ($\partial U / \partial T$) is defined as

$$\frac{\partial U}{\partial T} = \rho C_p \quad (38)$$

The variation of internal thermal energy per unit mass with respect to the spatial gradients of temperature ($\partial U / \partial \mathbf{g}$) is defined as

$$\frac{\partial U}{\partial \mathbf{g}} = -\dot{s} \rho C_p \Delta t - \dot{m}_g'' C_{pg} \Delta t \quad (39)$$

With Eq. (35), the variation of heat flux vector with respect to

temperature ($\partial \mathbf{f} / \partial T$), and the variation of the heat flux vector with respect to the spatial gradients of temperature ($\partial \mathbf{f} / \partial \mathbf{g}$) are defined as follows.

$$\frac{\partial \mathbf{f}}{\partial T} = 0 \quad (40)$$

$$\frac{\partial \mathbf{f}}{\partial \mathbf{g}} = -k \quad (41)$$

Thermal conductivity (k) can be a tensor for an anisotropic material. The gas diffusion equation (Eq. (9)) can also be implemented in ABAQUS, similar to the heat transfer equation. \dot{U} and \mathbf{f} of gas diffusion equation are as follows.

$$\dot{U} = -\frac{\partial \rho}{\partial t} \quad (42)$$

$$\mathbf{f} = -\frac{\rho_g \kappa}{\mu \phi} \nabla P \quad (43)$$

As pressure is treated as an imaginary temperature in the gas diffusion analysis, $\partial U / \partial T$ is $\partial U / \partial P$, $\partial \mathbf{f} / \partial T$ is $\partial \mathbf{f} / \partial P$, and $\mathbf{g} = \nabla P$.

The incremental form of Eq. (42) is

$$\Delta U = -\Delta \rho \quad (44)$$

Moreover, the internal thermal energy per unit mass at the end of the

increment (U) is defined using Eq. (37).

Assuming that the density of solid material does not affect pressure,

$$\frac{\partial U}{\partial P} = 0 \quad (45)$$

$$\frac{\partial U}{\partial \mathbf{g}} = 0 \quad (46)$$

Assuming that pyrolysis gas is an ideal gas,

$$\rho_g = \frac{PM_g}{RT} \quad (47)$$

M_g is molar mass of pyrolysis gas, and R is the ideal gas constant.

Combining Eq. (47) and (43) yields,

$$\frac{\partial f}{\partial P} = -\frac{M_g}{RT} \frac{\kappa}{\mu\phi} \nabla P \quad (48)$$

$$\frac{\partial f}{\partial \mathbf{g}} = -\frac{\rho_g \kappa}{\mu\phi} \quad (49)$$

-DISP

DISP subroutine is used to define the size of a prescribed boundary condition. This subroutine is used to specify the pressure boundary condition of the gas diffusion analysis domain.

-DFLUX

DFLUX subroutine defines a non-uniform flux that varies with

location, time, temperature, etc. In this study, it is used to specify the heat flux vector \mathbf{f} at the heating surface obtained through the surface energy balance equation (Eq. (19)) in the heat transfer analysis domain. The parameters constituting Eq. (19) are calculated in this subroutine. $\rho_e U_e C_H$ and h_r are predefined input parameter. σ , ε , and T_∞ are constant. Calculation of B_g' needs \dot{m}_g'' value as Eq. (18) and \dot{m}_g'' is flux vector \mathbf{f} at gas diffusion domain. DFLUX is called at the heat transfer domain so \dot{m}_g'' calculated in gas diffusion domain UMATHT is shared through common block. B_c' and h_w are determined by T_w , P , and B_g' and the relationship can be calculated using the NASA CEA database [64]. Pre-calculated relationship is available in the TACOT database. B' is obtained by adding B_c' and B_g' according to Eq. (18). The Stanton number C_H strongly depends on mass flux so it should be corrected as follows [65].

$$\frac{C_H}{C_{H0}} = \frac{\ln(1 + 2\lambda B')}{2\lambda B'} \quad (50)$$

Values of h_c and h_g depend on temperature is available on the TACOT database. Interpolation is performed to obtain the value at

the desired temperature.

With these values, the heat flux vector \mathbf{f} at the heating surface is defined.

$$\mathbf{f} = \rho_e U_e C_H (\dot{h}_r - \dot{h}_w) + \rho_e U_e C_H (B'_c \dot{h}_c + B'_g \dot{h}_g - B' \dot{h}_w) - \sigma \varepsilon (T_w^4 - T_\infty^4) \quad (51)$$

The recession velocity \dot{s} is calculated using the relations below and shared to subroutine UMESHMOTION using common block.

$$\dot{s} = \frac{\dot{m}_c}{\rho_s} \quad (52)$$

Also, \dot{m}_g'' correction due to surface recession is made in this subroutine.

-UMESHMOTION

UMESHMOTION subroutine is used when adaptive meshing is performed and is used to define the motion of nodes belonging to the adaptive mesh constraints node-set. Nodes belonging to the receding surface are designated as adaptive mesh constraints nodes, and through this subroutine, the recession of the desired speed can be simulated. The recession speed calculated from the DFLUX

subroutine is imported and the node displacement \mathbf{u} is defined using that value.

$$\mathbf{u}(t + \Delta t) = \mathbf{u}(t) + \dot{\mathbf{s}} \Delta t \quad (53)$$

When the receding surface node's position is determined, the positions of the remaining nodes in the adaptive mesh region are determined through the ABAQUS built-in Adaptive Lagrangian–Eulerian (ALE) method.

3. Nanoscale oxidation analysis of SiC ceramic using molecular dynamics simulation

3.1. Silicon Carbide (SiC) and Atomic Oxygen (AO)

Silicon Carbide (SiC) is one of the materials widely used in Ceramic Matrix Composite (CMC). It has low density, high-temperature capability, low thermal expansion, and high toughness, so it is used not only for non-ablative TPS but also for rocket nozzles and gas turbine components. In a high-temperature environment, oxygen molecules are decomposed into atomic oxygen (AO), and these AOs cause fatal damage to the material.

When AO collides with SiC, oxidation occurs, and oxidation of SiC is

more complicated than materials like Si because carbon is present [66]. Oxidation of SiC occurs in two ways, depending on temperature and pressure [67]. At low temperature and high oxygen pressure, solid SiO₂ layers are formed, and mass increases. The SiO₂ layer protects the SiC layer from further oxidation. On the other hand, gaseous species such as CO (g) are formed at high temperature and low pressure, and the protective layer begins to break down, so mass decreases. Due to these complex mechanisms, the oxidation of SiC requires profound research, but performing high energy AO collision experiments is very difficult and expensive. In this work, molecular dynamics was attempted as a substitute for experiments. In particular, the collision of SiC and AO was simulated using a reactive force field (Reaxff) to simulate a chemical reaction.

3.2. Molecular dynamics

Molecular dynamics is a simulation that predicts the movement of chemical particles such as molecules or atoms. Two atoms feel attraction at a long distance, but as they get closer, they will feel repulsive, as shown in Figure 7. John Lennard–Jones expressed this interatomic potential as the following Eq. (54) called the Lennard–

Jones (LJ) potential [68]. r is the distance between atoms, ϵ is the depth of the potential well

$$U_{LJ}(r) = 4\epsilon \left[\left(\frac{\sigma}{r} \right)^{12} - \left(\frac{\sigma}{r} \right)^6 \right] \quad (54)$$

The purpose of molecular dynamics is to predict atoms' motion over time in a numerical method, using this interatomic potential. If the potential between two atoms is known, the interaction force can be calculated through the derivative of the potential, and if the force is known, the acceleration of the two atoms can be calculated (Eq. (55)).

$$F = -\nabla U = ma \quad (55)$$

For numerical analysis, the motion of atoms is converted into discrete form and solved. The velocity and position of the atoms are calculated with known acceleration using Eq. (56) and (57), which are called the Verlet algorithm [69].

$$v(t + \Delta t) = v(t) + \frac{1}{2}a(t)\Delta t^2 \quad (56)$$

$$r(t + \Delta t) + r(t) = 2r(t) + a(t)\Delta t^2 \quad (57)$$

The accurate interatomic potential calculation is the most essential part of molecular dynamics, and pre-calculated potentials called force-fields such as PCFF [35], COMPASS [36], and ReaxFF [37]

are widely used.

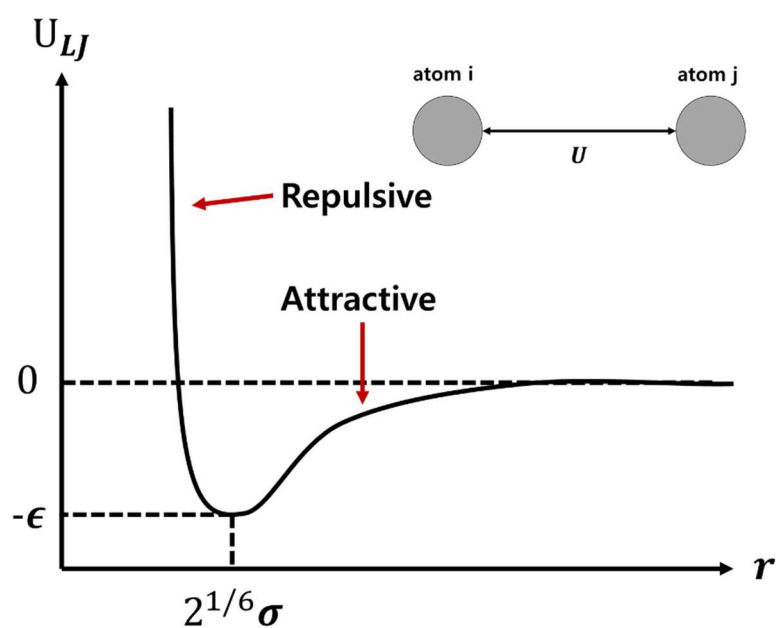


Figure 7 Typical graph of interatomic Lennard–Jones potential

3.3. Reaxff: The Reactive Force–Field

Classical force fields such as PCFF and COMPASS do not consider bond change between atoms, so they are not suitable for simulating ablation in which various reactions such as oxidation and degradation occur. On the other hand, Reaxff can simulate bond formation and destruction by using the distance between atoms. The bond order BO_{ij} between atom, i and atom j is obtained from the interatomic

distance r_{ij} using Eq. (58) and plotted in Figure 8 [37]. r_0 is the bond radii and $p_{bo,1\sim6}$ are the constant bond parameters determined by the type of atom. The first term is the sigma bond, the second term is the first pi bond, and the third is the second pi bond. Eq. (58) can be expressed up to bond order 3. The maximum bond order differs according to the types of interacting atoms.

$$BO'_{ij} = \exp \left[p_{bo,1} \cdot \left(\frac{r_{ij}}{r_0} \right)^{p_{bo,2}} \right] + \exp \left[p_{bo,3} \cdot \left(\frac{r_{ij}^\pi}{r_0} \right)^{p_{bo,4}} \right] \quad (58)$$

$$+ \exp \left[p_{bo,5} \cdot \left(\frac{r_{ij}^{\pi\pi}}{r_0} \right)^{p_{bo,6}} \right]$$

The recent ReaxFF force field developed by Vashisth et al. [67] is used in this work. This force field is not precisely for SiC oxidation, but parameters about Si/C/O are optimized and tested for the case of silicon oxycarbide ceramic material and verified the breakage of Si–O bond or Si–C bond.

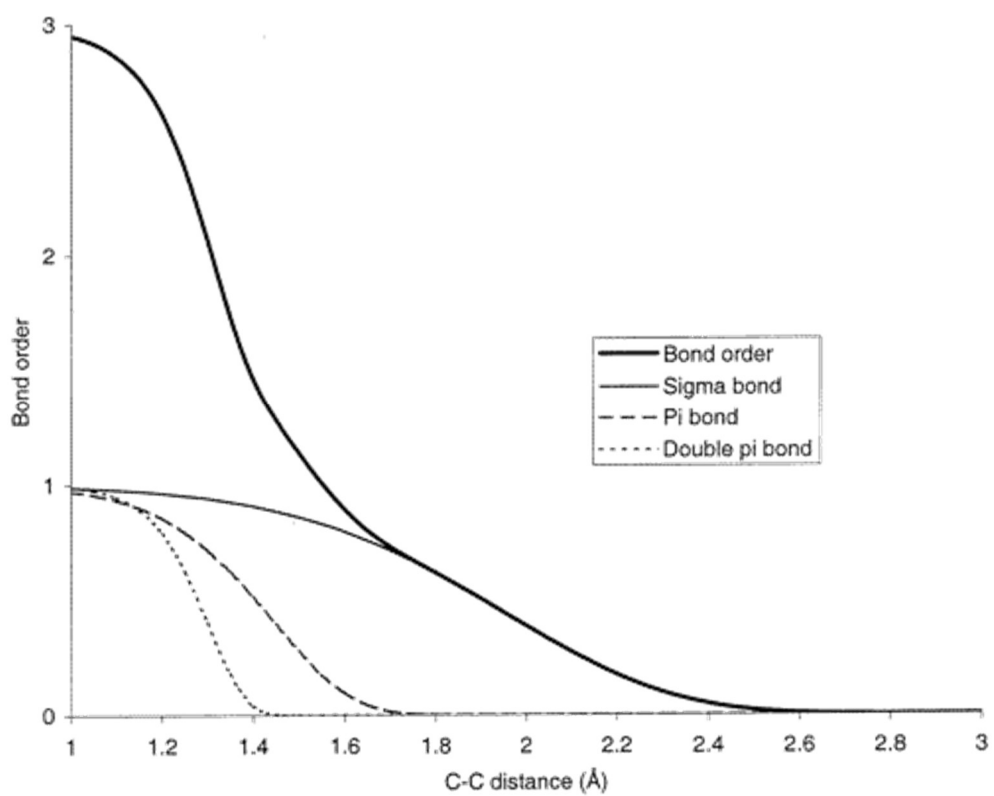


Figure 8 Interatomic distance dependency of the carbon-carbon bond order. Reprinted with permission from [37]. Copyright (2001) American Chemical Society.

3.4. Simulation Procedure

3.4.1. SiC structure modeling

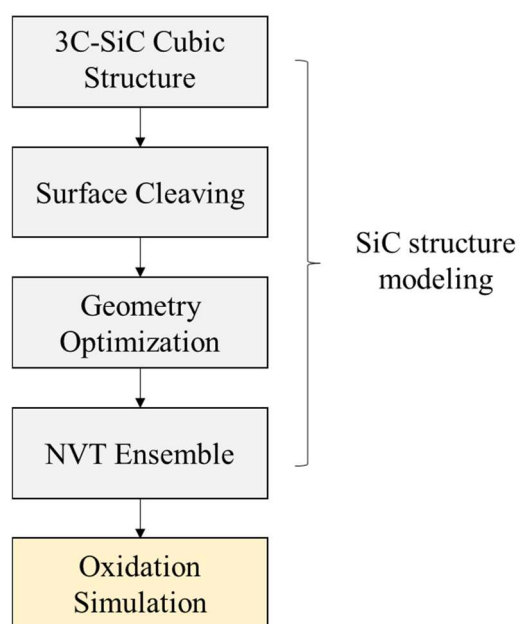


Figure 9 Procedure of SiC oxidation simulation

Figure 9 shows the procedure of SiC oxidation. Before oxidation simulation, an accurate atomic structure modeling is required. Here, a 3C-SiC crystal structure is made. SiC has 250 kinds of lattice structures, of which 3C-SiC is one of the significant SiC types [70]. 3C-SiC has a zinc blende crystal structure with a lattice constant of 4.3596 Å [71]. As shown in Figure 10 (a), the overall lattice structure

has a diamond lattice structure but contains two atoms of Si and C.

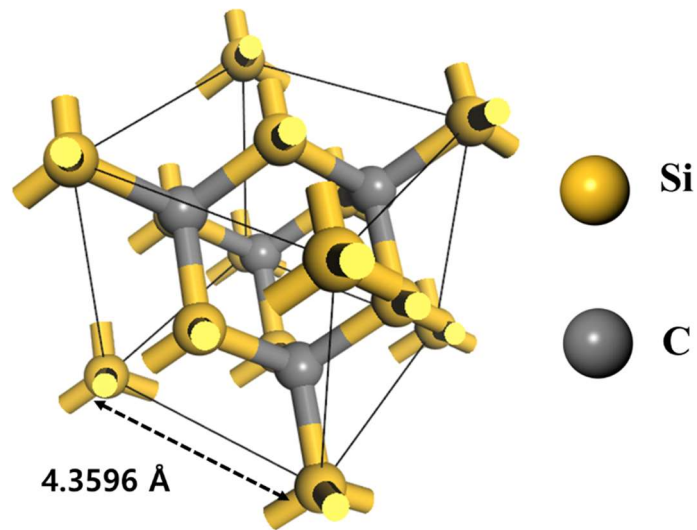


Figure 10 3C-SiC crystal structure

The bulk structure is made using the unit 3C-SiC crystal structure. Then, a surface to collide with an oxygen atom is created. At this time, three structures are made by adjusting the cleave angle. As shown in Figure 11, the atomic arrangement differs depending on which surface orientation cleaving is performed, which causes differences in material properties. The process up to this point is performed using commercial software Material Studio [72].

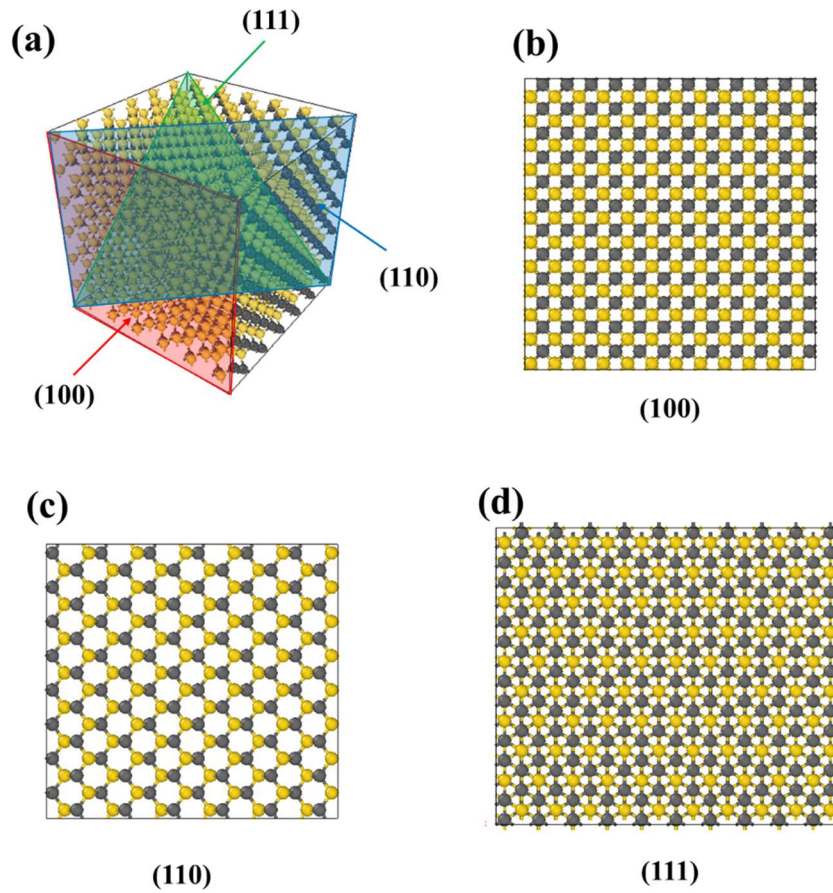


Figure 11 (a) Bulk 3C-SiC structure and top views of three different surface orientations: (100) (a), (110) (b), and (111) (c). Adapted with permission from [38]. Copyright (2020) American Institute of Aeronautics and Astronautics.

Structures are extracted and preprocessed to run on the open-source molecular dynamics simulation program LAMMPS [58]. A vacuum layer of a length of 15 \AA is made above the cleaved surface

as shown in Figure 12. Geometry optimization and NVT ensemble are conducted using LAMMPS to initialize and stabilize the structures. During geometry optimization, LAMMPS iteratively adjust coordinates of atoms to find local potential minimum to stabilize the structure. NVT ensemble, also known as canonical ensemble, means the possible state of the system with a constant number of atoms (N), volume (V), and temperature (T). Time integration of the equation of motion generates atoms' position and velocities with the desired temperature during the NVT ensemble. In this work, the NVT ensemble is conducted at 300K for 10ps to set the initial temperature. Table 1 shows the simulation box size, the number of atoms, and density after each orientation's NVT ensemble. It can be seen that the number of atoms differs depending on the orientation. This study assumes that the simulation boxes are repeated periodically in the x and y directions. To ensure the periodicity of structures with different atomic arrangements, it is hard to create a simulation box with the same number of atoms. The structures with little difference in the number of atoms while maintaining the periodic condition are used in this study. Due to the difference in the atomic arrangement

and the absence of periodicity in the z -axis caused by the vacuum layer's presence, the densities after the NVT ensemble show slight differences from the actual value of 3.21 g/cm^3 [71].

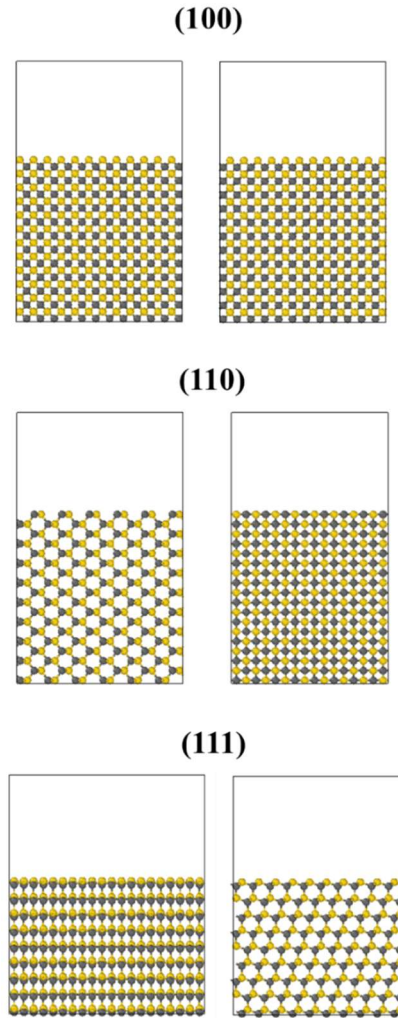


Figure 12 Preprocessed initial structures with different surface orientations. Adapted with permission from [38]. Copyright (2020) American Institute of Aeronautics and Astronautics.

Table 1 Simulation box size and number of atoms for each orientation

Orientation	Box size (Å)	Number of atoms	Density (after 300K NVT)
(100)	26 × 26 × 41	1728	3.023
(110)	26 × 25 × 43	1728	3.035
(111)	30 × 27 × 38	1800	3.187

3.4.2. Oxidation simulation

In the real world, oxygen molecules are decomposed into atomic oxygens (AO) due to heat or UV, and then the AO collides with the TPS material. Since it is impossible to incorporate complex phenomena that include heating, AO generation, AO collision, and erosion in one simulation, this work simplified and focused on AO's collision.

Figure 13 shows the overall configuration of the simulation box. Two types of simulations are designed (Table 2). The first type is to see the effect of surface orientation on the oxidation of SiC, and oxygen atoms collide with SiC in the NVE ensemble state. During the NVE ensemble, time integration is performed to find new speeds and positions while maintaining a constant number of atoms (N), volume

(V), and energy (E), which means that energy conservation is guaranteed without other restrictions such as temperature or pressure. At this time, three SiC structures of (100), (110), and (111) orientations are used.

The second type is aimed at understanding the effect of temperature. After applying the NVT condition to SiC, oxygen collides, and the (100) structure is used as a representative. Simultaneously, simulations are conducted for a total of 5 cases, 600K, 900K, 1200K, 1800K, and 2000K. Consequently, simulations are performed for eight cases by combining both types.

In common, the simulation time step is 0.25 fs (femtosecond), and a periodic boundary condition is applied in the x and y directions and fixed without a periodic condition in the z-direction. AOs are shot at a speed of 7km / s toward the SiC structure every 0.2 ps from a position 15Å above the SiC surface. The x,y coordinates are arbitrarily determined. At this time, AO is under the NVE condition. When the collision interval of 0.2ps is applied, the oxygen atom flux is excessively high compared to the actual one. However, due to the limitation of computation power, the time scale of molecular dynamics

is nano-second, so it is practically difficult to implement the actual time scale. Therefore, it is necessary to find an appropriate condition considering accuracy and efficiency. The bottom layer of 2 \AA is fixed to prevent the movement of SiC itself. All atoms passing through the top layer are eliminated to simulate the loss of mass due to erosion. For analysis of the results, temperature, mass, molecular composition, and atoms' coordinates are extracted over time. Data are obtained by performing three simulations for each case and averaging these results.

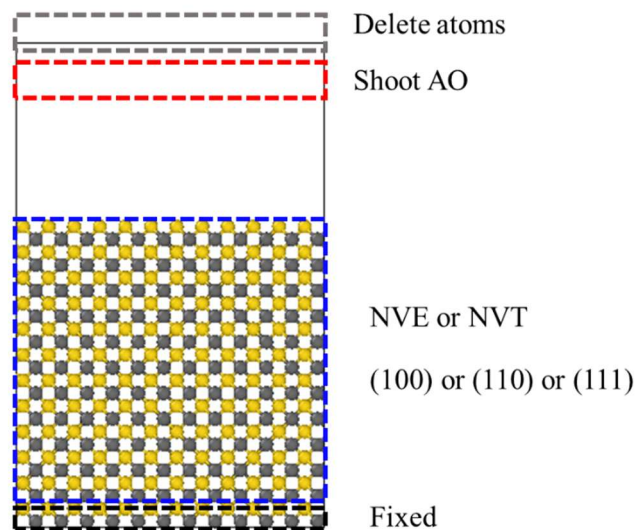


Figure 13 Overall configuration of the simulation box. Adapted with permission from [38]. Copyright (2020) American Institute of Aeronautics and Astronautics.

Table 2 Summary of simulation cases

Effect	Simulation condition
Surface orientation	NVE (100), (110), (111)
Temperature	NVT 600K, 900K, 1200K, 1800K, 2000K

4. Results and discussion

4.1. Verification of macro-scale ablation analysis of carbon/phenolic composite

To verify the implemented code, the test cases provided by the ablation workshop are used [73,74]. These test cases were produced to compare and verify different ablation analysis codes. The PATO program [75] developed by NASA, and the Amaryllis model embedded in commercial software SAMCEF, were verified using this test case. Test cases provide four different situations for a one-dimensional situation. A brief description is given in Table 3. The summary of the geometry and boundary conditions of the analysis model is shown in Figure 14. Two types of data are used to verify the code [74]. First type is about temperature response. Temperature

values of 10 points are obtained over time. Location of the points are top surface, 1mm, 2mm, 4mm, 8mm, 12mm, 16mm, 24mm, 50mm from the surface. The second type is pyrolysis and ablation response. Blowing rates of pyrolysis gas and char (\dot{m}_g'' , \dot{m}_c'') at the surface, pyrolysis zone thickness, depth of receding surface from the initial position are obtained. To find out pyrolysis zone thickness, location of pyrolysis and char fronts are estimated by finding the location where decomposition rate τ from Eq. (22) is 0.98 ($\rho_v(98\%) = \rho_c + 0.98(\rho_v - \rho_c)$) and 0.02 ($\rho_c(2\%) = \rho_c + 0.02(\rho_v - \rho_c)$). In this paper, obtained data are compared with output from PATO [75]. Figure 15 shows the temperature, pressure, and density contour of Case 1 at 60 seconds. Additionally, naive implementation of current code to 2D case is conducted.

Table 3 Summary of test case

Test case #	Description
1	No surface heat flux boundary condition, constant temperature boundary condition, constant pressure boundary condition, no recession
2	Low surface heat flux boundary condition, no temperature boundary condition, constant pressure boundary condition, no recession
3	Low surface heat flux boundary condition, no temperature boundary condition, constant pressure boundary condition, recession
4	High surface heat flux boundary condition, no temperature boundary condition, constant pressure boundary condition, recession

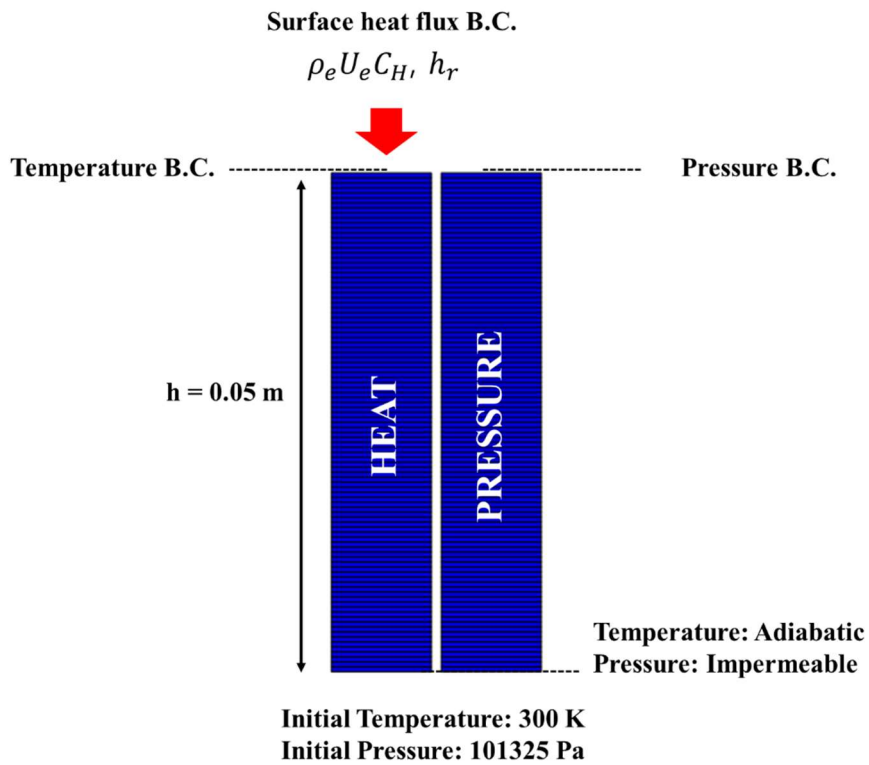


Figure 14 Geometry and boundary conditions of the analysis model

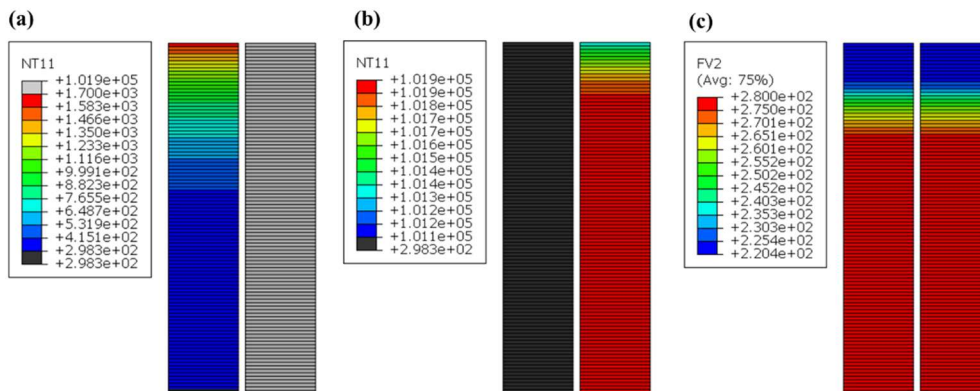


Figure 15 (a) Temperature, (b) pressure, and (c) density of Case 1 at 60 sec

4.1.1. Case 1: Constant temperature, no recession

Case 1 is a simple test case to compare the in-depth heat conduction and pyrolysis. The top side of the 5cm height TACOT material is being heated to 1664K for 1 minute under atmospheric pressure (101325 Pa). The bottom side is in the adiabatic and impermeable boundary condition. There is no recession. Figure 16 shows the temperature profile obtained from 10 different positions over time. Results from this work and PATO code are compared, and as shown, there are no differences between them. These results validate the in-depth heat conduction calculation scheme implemented in ABAQUS by using user subroutine. Blowing rates, pyrolysis zone, and recession profile are shown in Figure 17. In this case, a recession is neglected so \dot{m}_c and recession depth are zero. \dot{m}_g at the surface matches well with the result of PATO and this means that the gas diffusion analysis using a dual-domain system accurately predicts the movement of pyrolysis gas. Depth of ρ_v (98%) and ρ_c (2%) also shows no difference with PATO, which means that density calculation implemented in ABAQUS user subroutine using Arrhenius equation and explicit scheme can predict accurate density profile.

Table 4 Boundary condition of Case 1

Time (s)	T_w (K)	P_w (Pa)
0	298	101325
~60	1644	101325

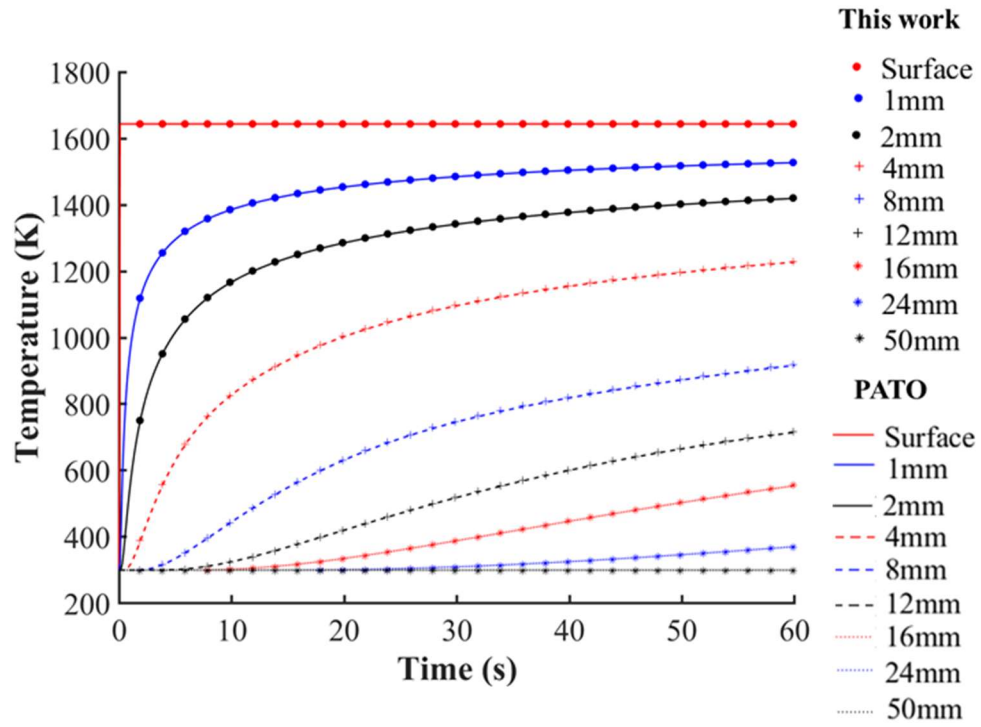


Figure 16 Case 1: Temperature profile (vs. PATO)

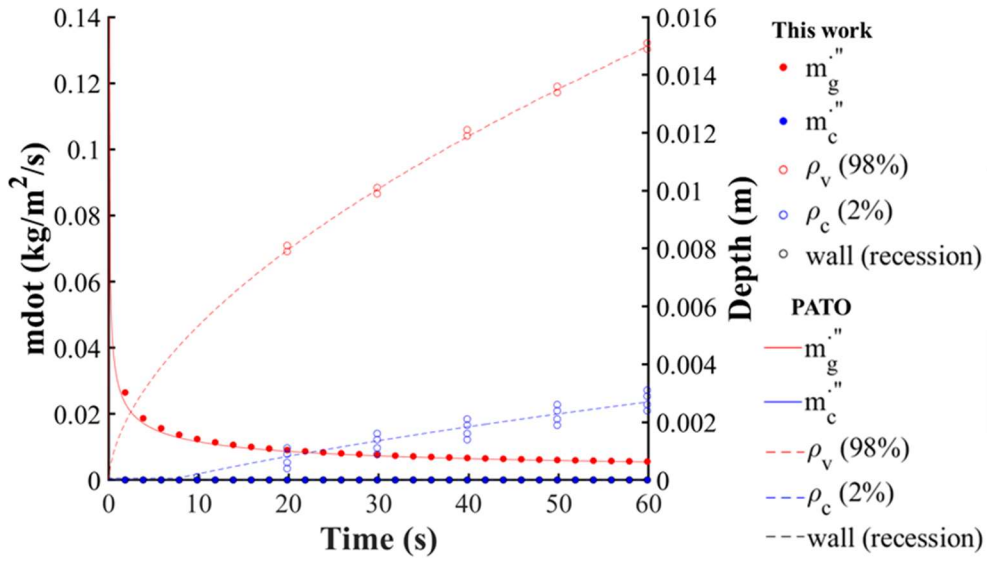


Figure 17 Case 1: Blowing rates, pyrolysis zone, and recession (vs. PATO)

4.1.2. Case 2: Low heating, no recession

Unlike the temperature boundary condition of Case 1, Case 2–4 have heat flux boundary conditions at the top surface. As shown in Figure 18, the heat transfer coefficient ($\rho_e U_e C_p$) and recovery enthalpy (h_r) change over time, and through this, the size of the heat flux boundary condition implemented in subroutine DFLUX using Eq. (51) varies. Heating proceeds for the first 60 seconds, and cooling proceeds for the remaining 60 seconds. The geometry and material model is the same as in Case 1. For cases 2 and 3, the exact boundary condition

values are in Table 5. The target surface temperature is about 1644K. There is no recession in Case 2. Figure 19 shows the temperature profiles of Case 2. Since the boundary condition is the heat flux, unlike Case 1, the surface temperature changes with time, and the present code shows the results highly consistent with the PATO. Figure 20 shows the blowing rates, pyrolysis zone, and recession profile of Case 2, and they also show high consistency with the PATO. Case 2 validate that the present code can predict the temperature, density, and gas movement accurately.

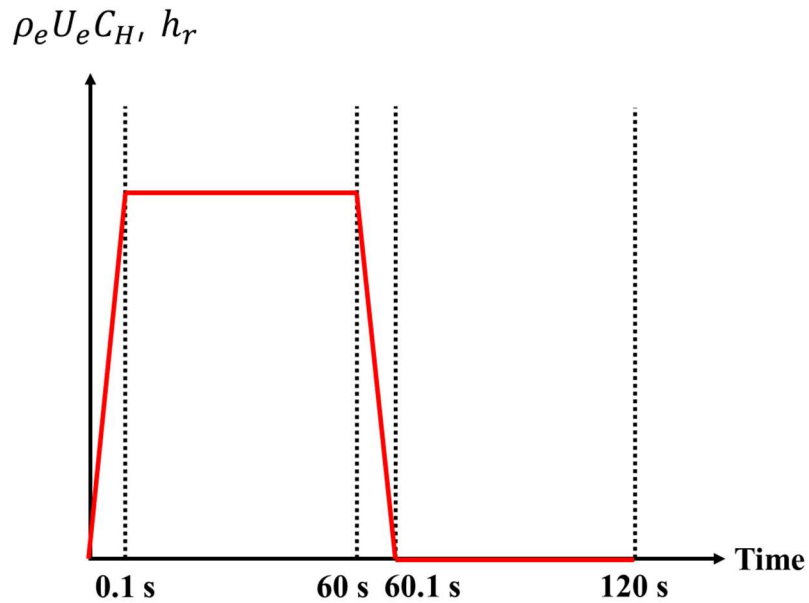


Figure 18 Heat flux boundary condition profile for Case 2-4

Table 5 Boundary condition of Case 2 and Case3

Time (s)	$\rho_e U_e C_H$ ($\text{kg} \cdot \text{m}^{-2} \cdot \text{s}^{-1}$)	h_r ($\text{J} \cdot \text{kg}^{-1}$)	p_w (Pa)
0	0	0	101325
0.1	0.3	$1.5 \cdot 10^6$	101325
60	0.3	$1.5 \cdot 10^6$	101325
60.1	0	0	101325
120	0	0	101325

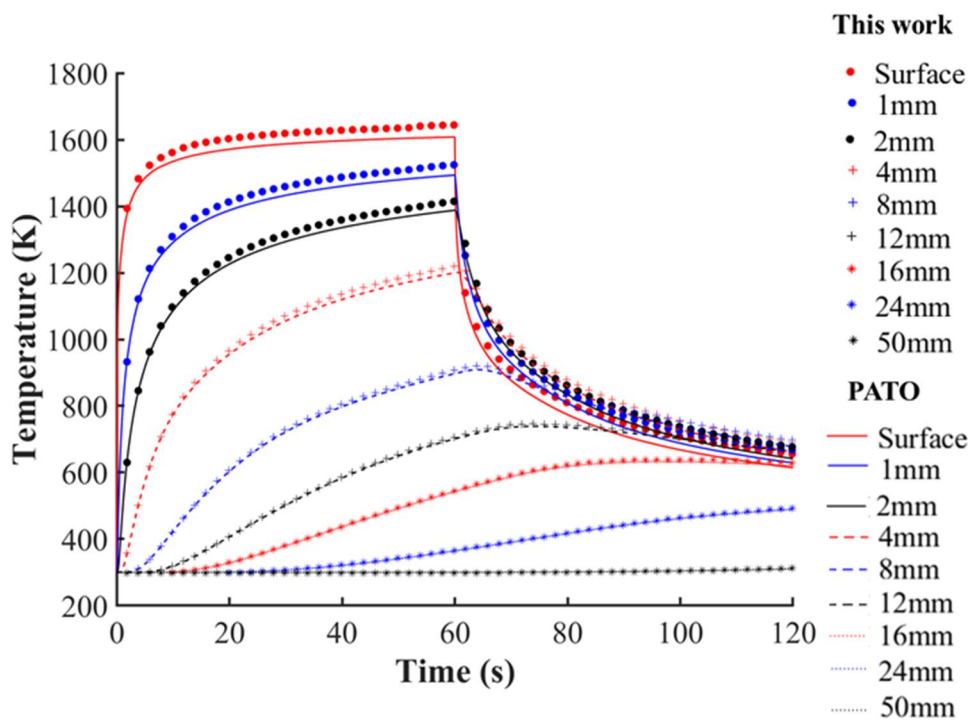


Figure 19 Case 2: Temperature profile (vs. PATO)

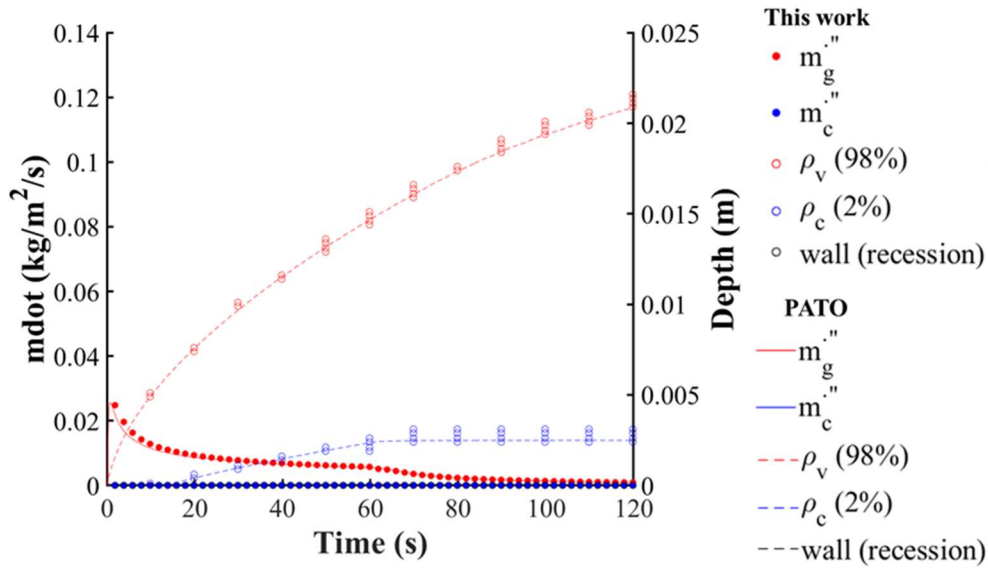


Figure 20 Case 2: Blowing rates, pyrolysis zone, and recession

4.1.3. Case 3: Low heating, recession

Case 3 includes a recession with the boundary condition of Case 2. During the analysis, the in-depth temperature probe points are fixed, but the surface temperature probe point moves along the receding surface. Figure 21 shows the temperature profile of Case 3. A sudden temperature drop means that the receding surface has moved below the corresponding probe point. Figure 22 shows the blowing rates, pyrolysis zone, and recession of Case 3. Not only the blowing rate of gas (\dot{m}_g) and depth of pyrolysis zone, but also the blowing rate of char (\dot{m}_c) and recession depth agree well with the PATO. This case

validates that the scheme using UMESHMOTION and ALE implements recession accurately in ABAQUS.

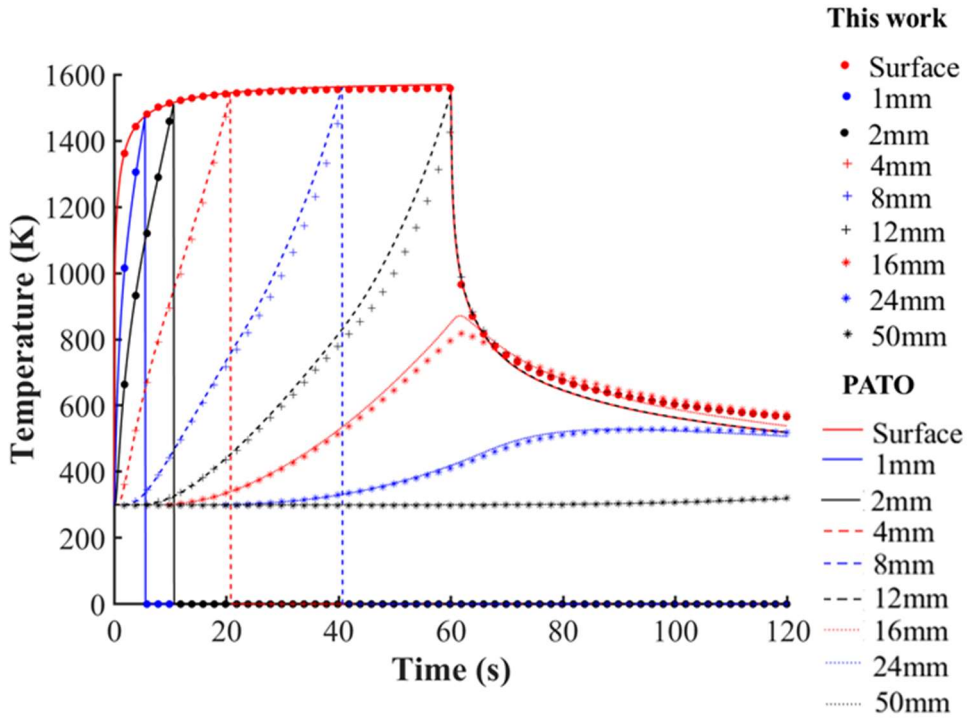


Figure 21 Case 3: Temperature profile (vs. PATO)

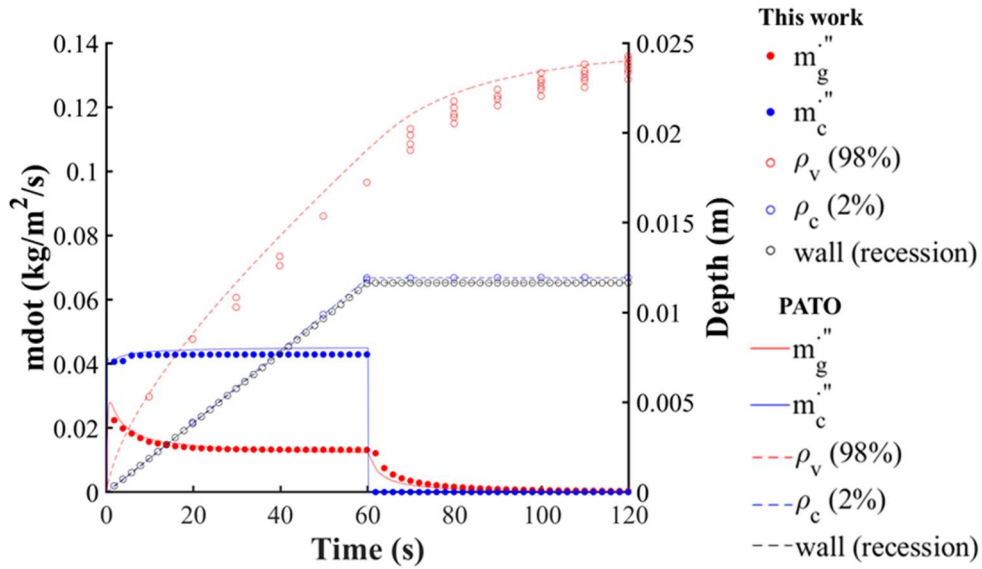


Figure 22 Case 3: Blowing rates, pyrolysis zone, and recession

4.1.4. Case 4: High heating, recession

In this case, recovery enthalpy (h_r) is higher than Case 2 and 3 (Table 6), and the target surface temperature is about 3000K. Temperature profiles of Case 4 are shown in Figure 23. The present code predicts temperature similarly to the PATO even in high heating case. It can be seen from Figure 24 that the blowing rates, pyrolysis zone, and recession are also similar to those of the PATO. The phenomenon that the thickness of the perfectly charred layer ($\rho_c(2\%) \sim \text{wall}(\text{recession})$) increased due to the higher temperature compared to Case 3 is observed.

Table 6 Boundary condition of Case 4

Time (s)	$\rho_e U_e C_H$ ($\text{kg} \cdot \text{m}^{-2} \cdot \text{s}^{-1}$)	h_r ($\text{J} \cdot \text{kg}^{-1}$)	p_w (Pa)
0	0	0	101325
0.1	0.3	$2.5 \cdot 10^7$	101325
60	0.3	$2.5 \cdot 10^7$	101325
60.1	0	0	101325
120	0	0	101325

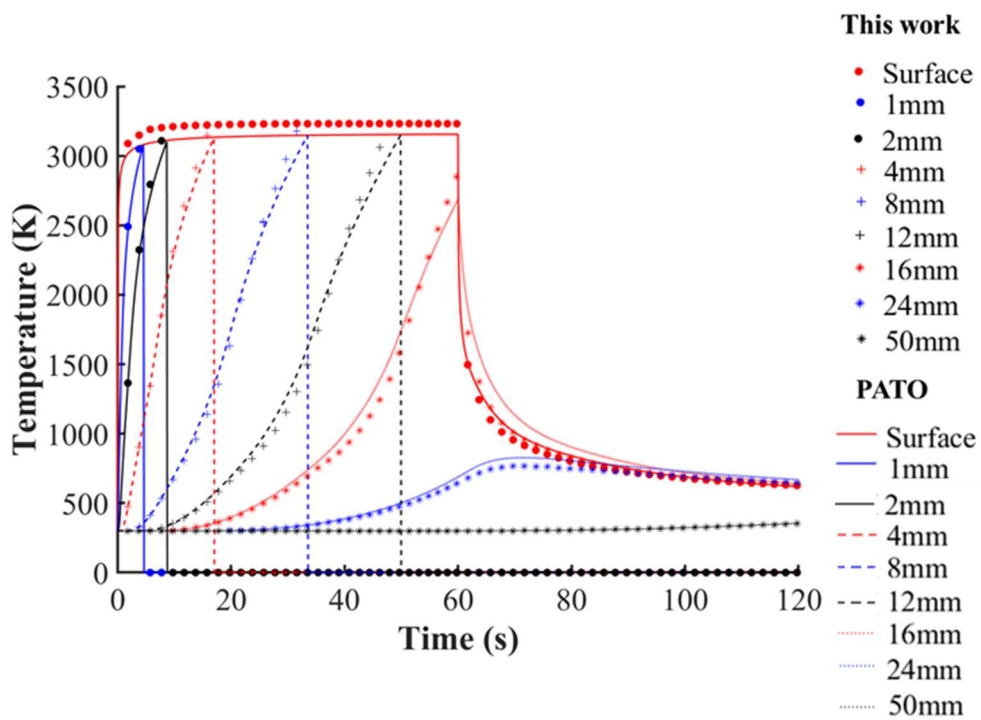


Figure 23 Case 4: Temperature profile (vs. PATO)

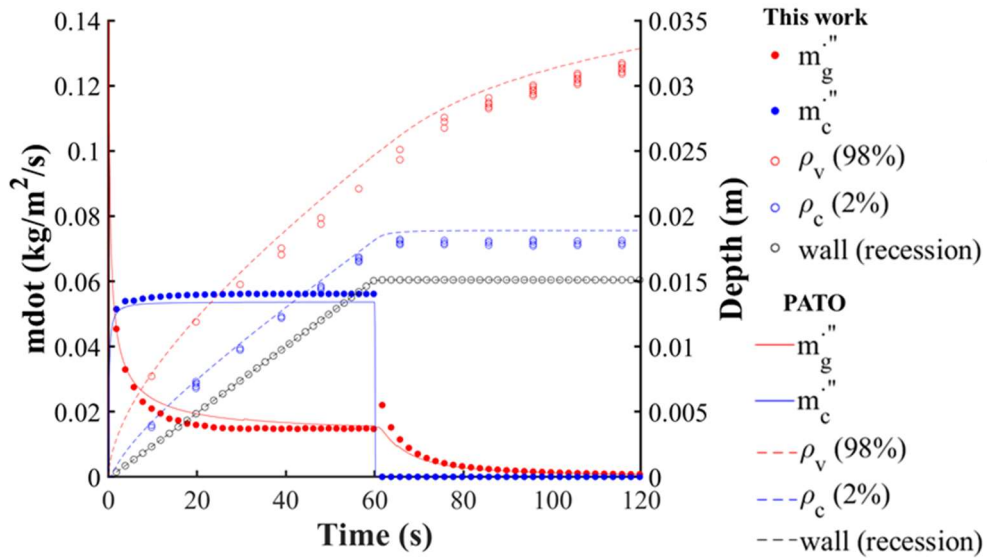


Figure 24 Case 4: Blowing rates, pyrolysis zone, and recession

4.1.5. Case 5: High heating, recession in 2D

The naive implementation of current code to the 2D case is conducted, and results are compared with ablation test case results [60]. The geometry of the 2D model is shown in Figure 25. Heat flux and pressure boundary conditions are applied at the top and right side surfaces. In this case, heat flux varies depending on the location. The q_w/q_{w0} value (heat flux/stagnation point heat flux) at each location can be found in the Table 7, and this scale factor is multiplied to the coefficient ($\rho_e U_e C_H$) at Table 8 to change the heat flux. Figure 26 shows the temperature, density, and pressure of case 5 at 40 seconds

and Figure 27 shows the temperature profile of points located vertically below the stagnation point. At points close to the surface, the temperature is the same as the reference. However, the deeper the depth is, the greater the difference is. The error's leading cause is that ABAQUS is a commercial finite element analysis program with limited changes that users can make. The user can change the governing equations, properties, and boundary conditions through the subroutine, but cannot change the solver's part. In particular, the ALE method used to simulate recession applies the moving boundary condition to the solution variable (temperature), but it does not seem to be applied to the other variables such as density.

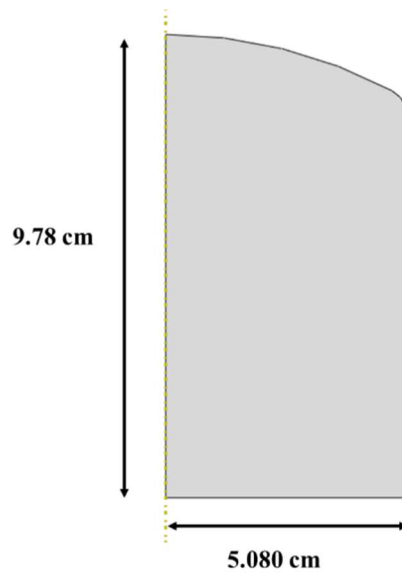


Figure 25 Geometry of 2D model

Table 7 Heat flux distribution depending on coordinate [60]

X	Y	q_w/q_{w0}	X	Y	q_w/q_{w0}
0.000	0.000	1	5.068	1.617	0.476
1.987	0.196	1	5.080	1.864	0.261
2.957	0.439	0.971	5.080	2.114	0.169
3.431	0.597	0.955	5.080	2.614	0.137
3.898	0.777	0.925	5.080	4.114	0.111
4.354	0.980	0.863	5.080	6.114	0.101
4.800	1.209	0.743	5.080	9.780	0.101

Table 8 Boundary condition of Case 5

Time (s)	$\rho_e U_e C_H$ ($\text{kg} \cdot \text{m}^{-2} \cdot \text{s}^{-1}$)	h_r ($\text{J} \cdot \text{kg}^{-1}$)	p_w (Pa)
0	0	0	101325
0.1	0.3	$2.5 \cdot 10^7$	101325
40	0.3	$2.5 \cdot 10^7$	101325
40.1	0	0	101325
120	0	0	101325

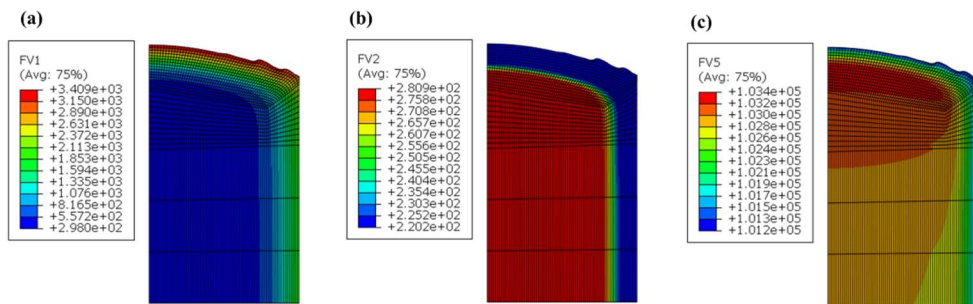


Figure 26 (a) Temperature, (b) density, and (c) pressure of Case 5 at 40 sec

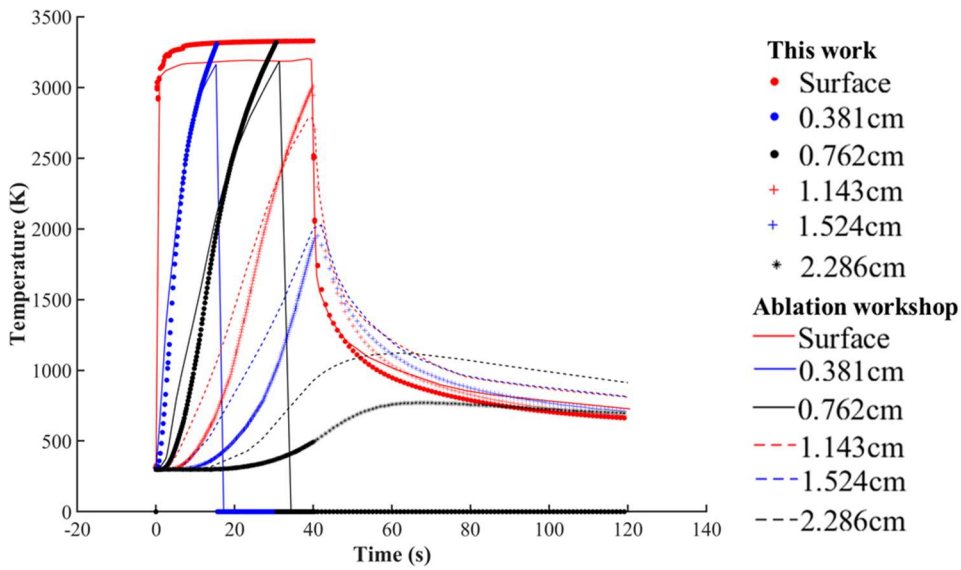


Figure 27 Temperature profile (vs. Ablation workshop [60])

4.2. Nanoscale oxidation analysis of SiC ceramic

4.2.1. Effect of surface orientation

Collision with AO causes a change in the structure of SiC, as shown in Figure 28. As shown in Figure 28, at the beginning of the simulation, AOs are mainly attached to the SiC surface in the form of silicon suboxide SiO_x (Figure 29 (a)), but as time passes, gaseous species such as $\text{CO}(\text{g})$ (Figure 29(b)) are formed, and after a specific time, SiC is wholly destroyed. Figure 31 shows the normalized mass of each surface orientation structure. As shown in Table 1, the number of atoms is different for each structure, so the results are compared

using normalized mass. Figure 31(a) shows the change in mass over the entire simulation time. At about the same time, rapid mass changes occur. Figure 31(b) shows the mass change during 0–25ps. In Figure 31(b), the results that are not well seen in Figure 31(a) can be found. The time for erosion to occur varies depending on the surface orientation. The (110) structure is eroded first; the (111) structure is then; and the (100) structure is eroded last. This can be explained by the difference in the number of Si–C bonds holding surface carbon. Figure 30 shows the bonding structures of surface carbon according to the surface orientation. The (110) structure has three bonds, and the (100) and (111) structures have four bonds. The higher the number of bonds, the better the carbon adheres to the surface, and the erosion decreases. Thus, the (110) structure is eroded first. The (100) structure and the (111) structure have the same number of bonds. However, as seen in the structure of 0 ps of Figure 28, in the (100) structure, the surface carbon is entirely covered by Si, but the carbon of the (111) structure is slightly exposed on the surface. This difference is expected to cause the (111) structure to erode faster. Many studies have experimentally

verified that C-face SiC is oxidized faster than Si-face SiC and is consistent with this study [76–78].

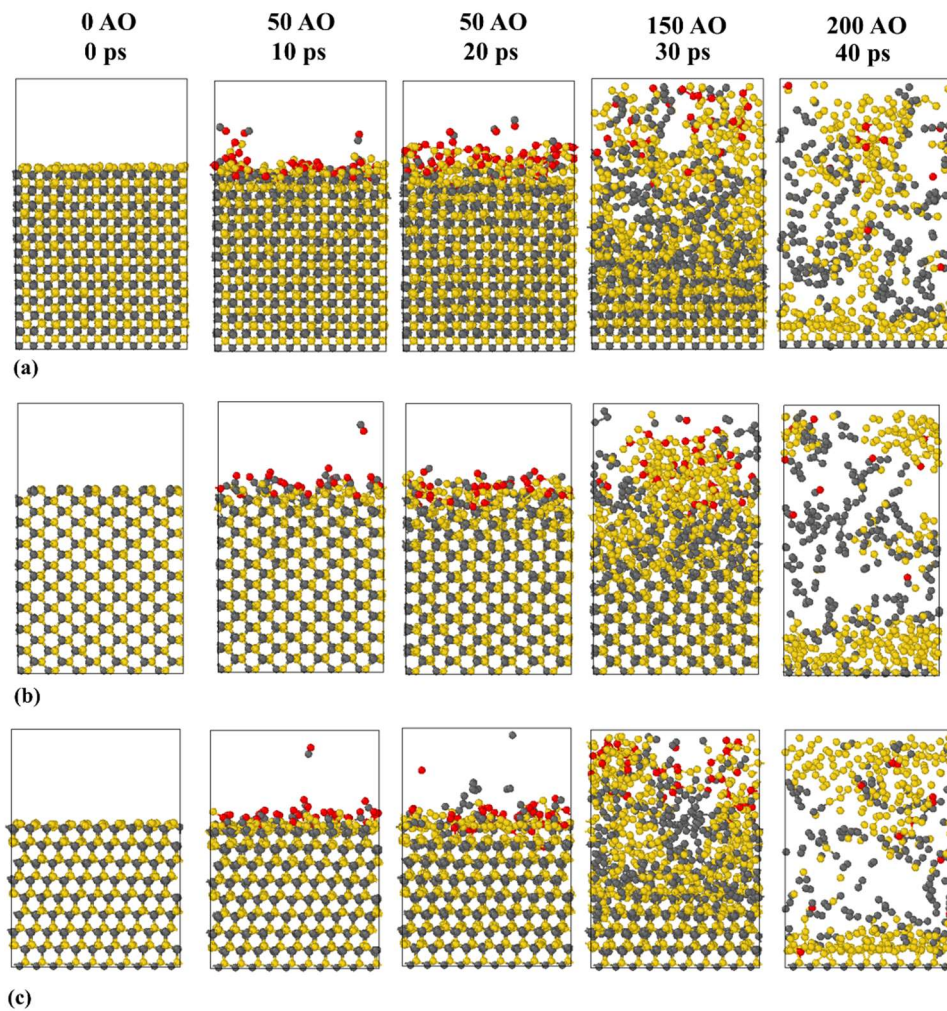


Figure 28 Structural changes of (a) (100), (b) (110), and (c) (111) SiC after AO collision. Adapted with permission from [38]. Copyright (2020) American Institute of Aeronautics and Astronautics.

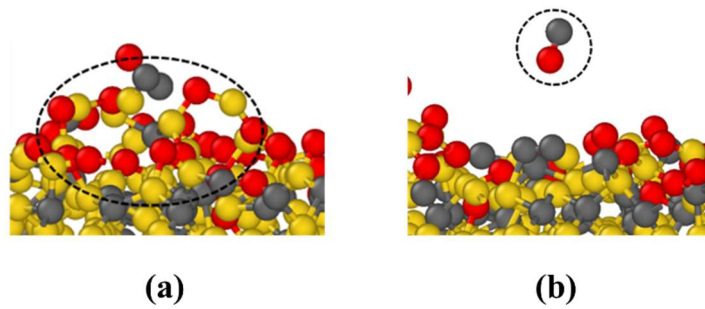


Figure 29 Products formed due to AO collision: a) amorphous SiO_x, and (b) CO(g). Adapted with permission from [38]. Copyright (2020) American Institute of Aeronautics and Astronautics.

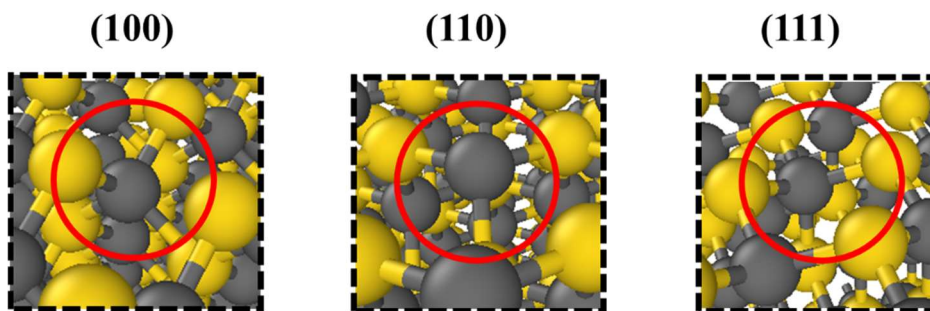


Figure 30 Surface carbon bonding structures. Adapted with permission from [38]. Copyright (2020) American Institute of Aeronautics and Astronautics.

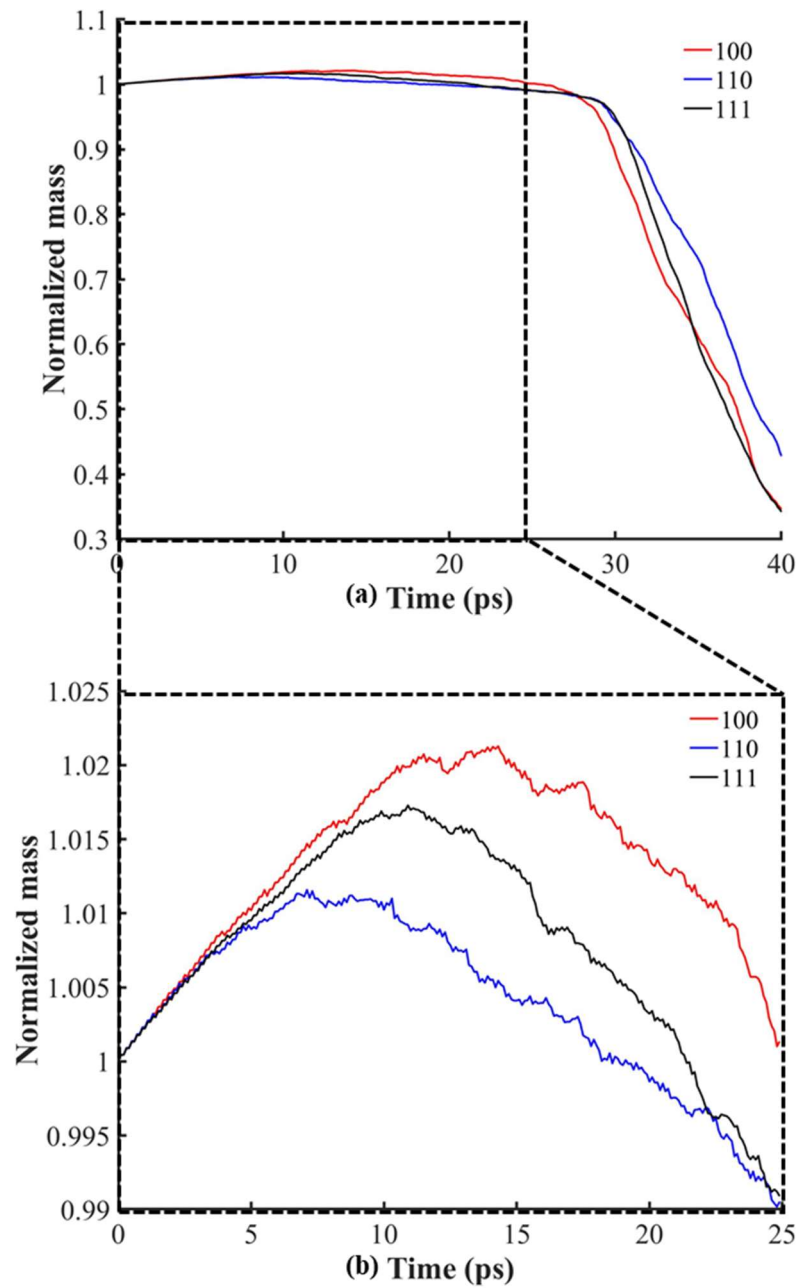


Figure 31 Mass profiles (a) from 0 to 40ps and (b) 0 to 25 ps. Adapted with permission from [38]. Copyright (2020) American Institute of Aeronautics and Astronautics.

4.2.2. Effect of temperature

The effect of temperature on the oxidation of SiC is analyzed using the (100) structure. Figure 32(a) shows the temperature and normalized mass in the simulation box over the entire simulation time. The blue line in Figure 32 shows the temperature of (100) SiC when the AO collision continues under NVE conditions. The high kinetic energy of AO with a speed of 7 km/s is transmitted to SiC through collision and causes the atoms to vibrate to raise the temperature. The red line is the normalized mass of (100) SiC. First, oxidation and sublimation are observed. The temperature increases linearly up to 3300K, then decreases rapidly. The linear temperature region is the oxidation zone, and the sublimation region after that.

As shown in 30 and 40 ps in Figure 28, the entire SiC lattice structure collapses, and atoms escape the simulation box. As it is clearly distinguished from previous partial damage, this phenomenon is concluded as sublimation by high temperature, not oxidation. As the atoms exit the simulation box, the atoms' energy disappears, reducing the energy of the entire system, resulting in an abrupt decrease in temperature. The sublimation temperature observed in this result

(3300K) is higher than the experimental value of 3000K (2730°C) [67]. In LAMMPS, the temperature is obtained through the kinetic energy of the atoms. Since the erode atoms in the current simulation configuration do not immediately exit the simulation box, it is assumed that their high kinetic energy is included in the calculation, and the sublimation temperature is measured higher than the experimental value.

Figure 32 (b) shows the normalized mass and temperature in the oxidation region. The oxidation region is again divided into two regions: passive oxidation and active oxidation. The passive to active transition, in which the mass increases at low temperature and decreases at a specific temperature, can be confirmed through Figure 32 (b). As mentioned earlier, in the passive oxidation, the mass increases at low temperature and high pressure. In the active oxidation, mass decreases at high temperature and low pressure. In this study, the pressure condition is assumed to be constant because the interval at which AO collides with SiC is constant. Therefore, it is concluded that the cause of the transition is temperature. The main reason for the mass change is the formation of CO(g) molecules.

When AO collides with SiC, it mainly reacts with Si to form an oxide, but some AOs combine with the carbon and prepare to become CO(g). At low temperatures, the energy is insufficient, and it cannot escape in the form of a gas, but when the temperature increases, it gains energy, becomes a gas, and flies away. As shown in Figure 33, the point at which the mass decreases and the peak point of the number of CO(g) molecules coincide. The number of CO(g) molecules shows a peak because the CO(g) molecules have been generated and then exited the simulation box. The number of initially generated CO(g) molecules is small, so the effect on mass is insignificant. As the temperature increases, the number increases, and the overall mass decreases.

To clarify the effect of oxidation on temperature, AO collision simulation is additionally performed under NVT conditions. Only the results of the first 10ps are analyzed to determine the tendency of the initial oxidation. Figure 34 shows the mass change of (100) SiC during AO collision under various temperature conditions (600, 900, 1200, 1800, and 2000K). The results under the NVE condition of Figure 32 (b) and the results under the NVT condition of Figure 34

show consistency. At temperatures of 600K and 900K, the mass continues to increase. There is a slight reduction in mass at 1200K, but no significant effect. However, mass reduction increases from 1800K, and rapid mass decrease is seen at 2000K. From these results, we confirm that temperature influences the oxidation of SiC.

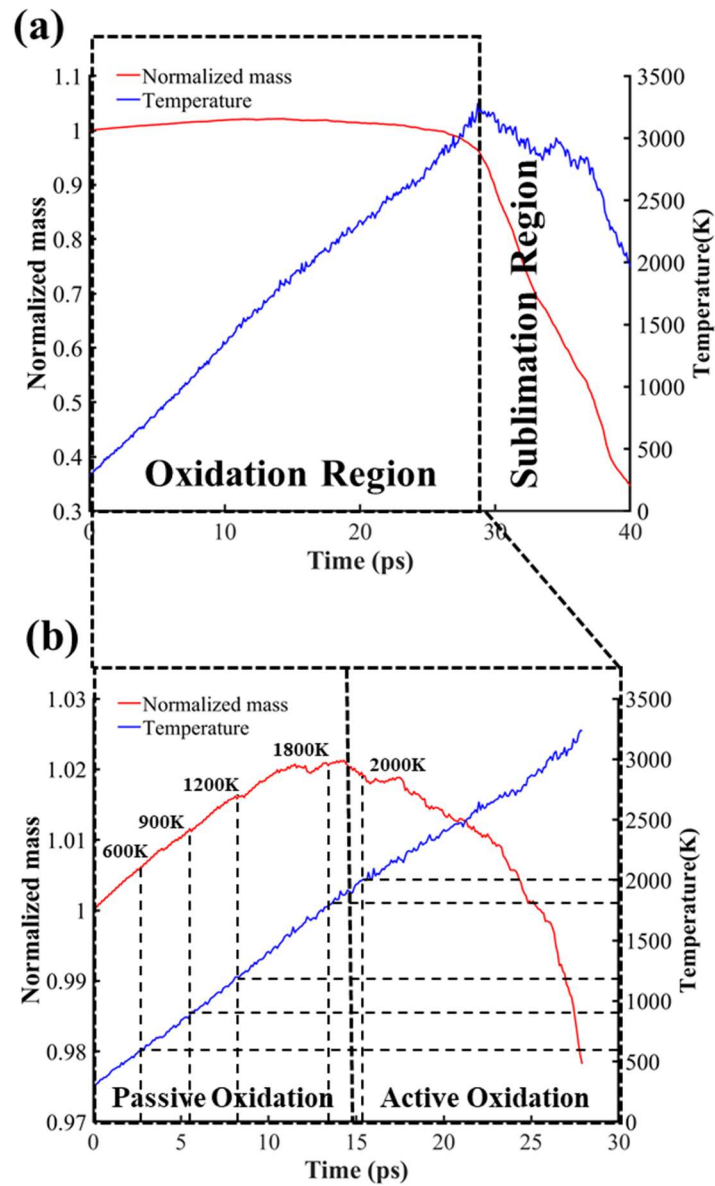


Figure 32 Normalized mass and temperature profile of (100) SiC structure (a) over the entire simulation time, and (b) in the oxidation mass region. Adapted with permission from [38]. Copyright (2020) American Institute of Aeronautics and Astronautics.

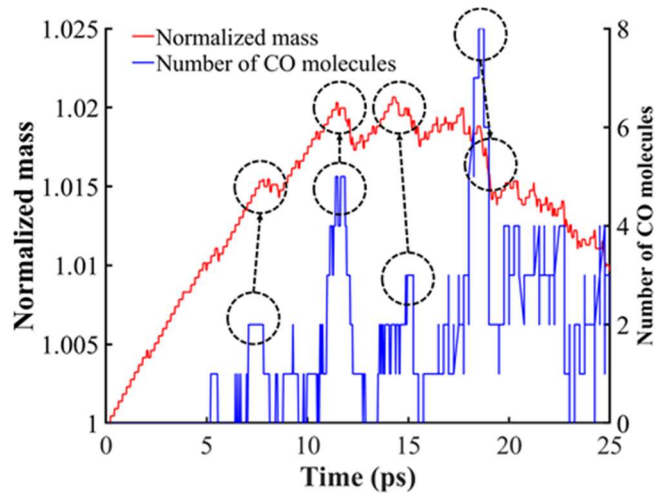


Figure 33 Normalized mass and number of CO molecules in the oxidation. Adapted with permission from [38]. Copyright (2020) American Institute of Aeronautics and Astronautics.

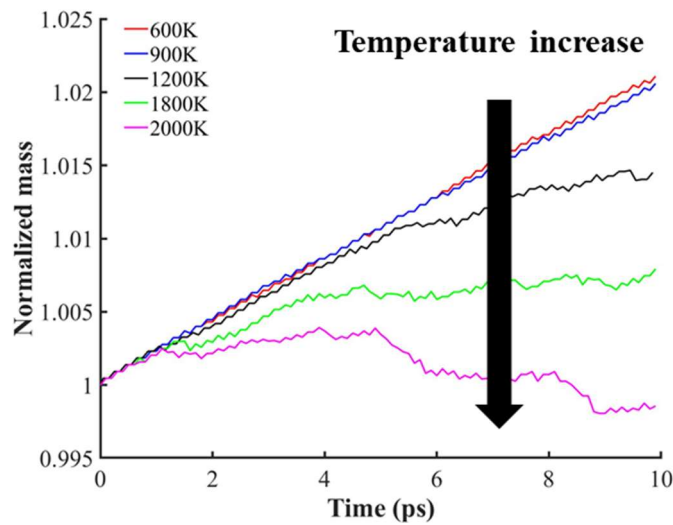


Figure 34 Normalized mass of SiC during initial AO collision (0–10ps) at various temperatures. Adapted with permission from [38]. Copyright (2020) American Institute of Aeronautics and Astronautics.

5. Conclusions and future works

5.1. Conclusions

In this thesis, macro-scale carbon/phenolic composite ablation analysis using finite element analysis and nanoscale SiC oxidation analysis using molecular dynamics are conducted as a fundamental study for multi-scale analysis.

In the case of macro-scale analysis, in-depth heat transfer and gas diffusion, material decomposition, and surface heat flux boundary condition are implemented to commercial finite element software ABAQUS using USERSUBROUTINE. A dual domain system is used to analyze heat transfer and gas diffusion simultaneously. The physical properties of the material were obtained using the open-source database TACOT. Temperature, density, and gas movements are obtained under various surface boundary conditions (constant temperature, low heat flux, high heat flux) and verified with open-source ablation code PATO.

In nanoscale analysis, the influence of surface orientation and temperature on the oxidation of SiC is analyzed through reactive MD simulation. A simulation is performed in which oxygen atoms collide

with SiC structures having different surface orientations [(100), (110), (111)] under NVE conditions, and the (110) structure showed the highest reactivity. The cause of this phenomenon is explained through the number of Si–C bonds in the surface carbon. Besides, the oxidation transition according to temperature is observed by analyzing the results of the AO collision simulation under the NVE condition of the (100) structure, and the difference in oxidation rate according to the temperature is verified through NVT simulations at different temperatures (600, 900, 1200, 1800, and 2000 K).

5.2. Future works

In the case of macro–scale analysis, as the commercial finite element program ABAQUS is used, there are many possibilities that it can be expanded to multi–physics analysis such as combined thermal–structure analysis or thermal–flow analysis. Based on the problems identified in naive 2D implementation, the code should be improved so that the interpretation of complex multidimensional shapes is possible.

In nanoscale analysis, the simulation results show similar tendencies compared with experiments. However, due to the limitations of the

MD's time and length scale, it is not entirely consistent with the experimental values. It is necessary to develop a simulation technique that can improve accuracy and efficiency by overcoming these scale discrepancies' limitation.

This study aims to construct an analysis framework at each scale as a preliminary study for multiscale analysis. Therefore, the analysis methodology at various scales between macro and nano must also be studied. Besides, the development of a scale bridging method to link the results from the various scale is essential.

Reference

- [1] Anderson Jr, J. D. *Hypersonic and High-Temperature Gas Dynamics*. Americal Institute of Aeronautics and Astronautics, 2006.
- [2] NASA Content Administrator. Soyuz Re-Entry. *NASA*.
https://www.nasa.gov/multimedia/imagegallery/image_feature_2397.html.
- [3] Smith, Y. Heat Shield Milestone Complete for First Orion Mission with Crew. *NASA/Isaac Watson*. <https://www.nasa.gov/image-feature/heat-shield-milestone-complete-for-first-orion-mission-with-crew>.
- [4] Natali, M., Kenny, J. M., and Torre, L. “Science and Technology of Polymeric Ablative Materials for Thermal Protection Systems and Propulsion Devices: A Review.” *Progress in Materials Science*, Vol. 84, 2016, pp. 192–275.
<https://doi.org/10.1016/j.pmatsci.2016.08.003>.
- [5] Tran, H. K., Johnson, C., Rasky, D., Hui, F., Hsu, M. T., Chen, T., Chen, Y. K., Paragas, D., and Kobayashi, L. “Phenolic Impregnated Carbon Ablators PICA as Thermal Protection System for Discovery Missions.” *NASA TM-110440*, 1997.
- [6] Edquist, K. T., Hollis, B. R., Johnston, C. O., Bose, D., White, T. R., and Mahzari, M. “Mars Science Laboratory Heat Shield Aerothermodynamics: Design and Reconstruction.” *Journal of Spacecraft and Rockets*, Vol. 51, No. 4, 2014, pp. 1106–1124.
<https://doi.org/10.2514/1.A32749>.
- [7] Linda, H. Heat Shield Install Brings Orion Spacecraft Closer to Space. *NASA's John F. Kennedy Space Center*.
<https://www.nasa.gov/feature/heat-shield-install-brings-orion->

spacecraft—closer—to—space.

- [8] Graves Jr, R. A., and Witte, W. G. “Flight Test Analysis of Apollo Heat Shield Material Using the Pacemaker Vehicle System.” *NASA Technical Note D-4713*, 1968, p. 8.
- [9] Fahrenholtz, W. G., and Hilmas, G. E. “Ultra-High Temperature Ceramics: Materials for Extreme Environments.” *Scripta Materialia*, Vol. 129, 2017, pp. 94–99.
<https://doi.org/10.1016/j.scriptamat.2016.10.018>.
- [10] Opeka, M. M., Talmy, I. G., Wuchina, E. J., Zaykoski, J. A., and Causey, S. J. “Mechanical, Thermal, and Oxidation Properties of Refractory Hafnium and Zirconium Compounds.” *Journal of the European Ceramic Society*, Vol. 19, Nos. 13–14, 1999, pp. 2405–2414. [https://doi.org/10.1016/s0955-2219\(99\)00129-6](https://doi.org/10.1016/s0955-2219(99)00129-6).
- [11] Zhang, X., Luo, X., Han, J., Li, J., and Han, W. “Electronic Structure, Elasticity and Hardness of Diborides of Zirconium and Hafnium: First Principles Calculations.” *Computational Materials Science*, Vol. 44, No. 2, 2008, pp. 411–421.
<https://doi.org/10.1016/j.commat.2008.04.002>.
- [12] Eakins, E., Jayaseelan, D. D., and Lee, W. E. “Toward Oxidation-Resistant ZrB₂-SiC Ultra High Temperature Ceramics.” *Metallurgical and Materials Transactions A: Physical Metallurgy and Materials Science*, Vol. 42, No. 4, 2011, pp. 878–887.
<https://doi.org/10.1007/s11661-010-0540-8>.
- [13] Zhang, X., Hu, P., Han, J., and Meng, S. “Ablation Behavior of ZrB₂-SiC Ultra High Temperature Ceramics under Simulated Atmospheric Re-Entry Conditions.” *Composites Science and Technology*, Vol. 68, Nos. 7–8, 2008, pp. 1718–1726.
<https://doi.org/10.1016/j.compscitech.2008.02.009>.

- [14] Hwang, S. S., Vasiliev, A. L., and Padture, N. P. “Improved Processing and Oxidation–Resistance of ZrB₂ Ultra–High Temperature Ceramics Containing SiC Nanodispersoids.” *Materials Science and Engineering A*, Vol. 464, Nos. 1–2, 2007, pp. 216–224. <https://doi.org/10.1016/j.msea.2007.03.002>.
- [15] Fahrenholtz, W. G. “Thermodynamic Analysis of ZrB₂–SiC Oxidation: Formation of a SiC–Depleted Region.” *Journal of the American Ceramic Society*, Vol. 90, No. 1, 2007, pp. 143–148. <https://doi.org/10.1111/j.1551-2916.2006.01329.x>.
- [16] Bartlett, E. P., Kendall, R. M., Moyer, C. B., and Rindal, R. A. “An Analysis of the Coupled Chemically Reacting Boundary Layer and Charring Ablator, Part 1 Summary Report.” *NASA Contractor Report*, 1968.
- [17] Moyer, C. B., and Rindal, R. A. “An Analysis of the Coupled Chemically Reacting Boundary Layer and Charring Ablator. Part 2–Finite Difference Solution for the in–Depth Response of Charring Materials Considering Surface Chemical and Energy Balances.” *NASA Contractor Report*, 1968.
- [18] Bartlett, E. P., and Kendall, R. M. “An Analysis of the Coupled Chemically Reacting Boundary Layer and Charring Ablator. Part 3–Nonsimilar Solution of the Multicomponent Laminar Boundary Layer by an Integral Matrix Method.” *NASA Contractor Report*, 1968.
- [19] Bartlett, E. P., Kendall, R. M., and Rindal, R. A. “An Analysis of the Coupled Chemically Reacting Boundary Layer and Charring Ablator. Part 4–A Unified Approximation for Mixture Transport Properties for Multicomponent Boundary–Layer Applications.” *NASA Contractor Report*, 1968.
- [20] Kendall, R. M. “An Analysis of the Coupled Chemically Reacting

- Boundary Layer and Charring Ablator. Part 5–A General Approach to the Thermochemical Solution of Mixed Equilibrium–Nonequilibrium, Homogeneous or Heterogeneous Systems.” *NASA Contractor Report*, 1968.
- [21] Rindal, R. A. “An Analysis of the Coupled Chemically Reacting Boundary Layer and Charring Ablator. Part 6–An Approach for Characterizing Charring Ablator Response with in–Depth Coking Reactions.” *NASA Contractor Report*, 1968.
- [22] Moyer, C. B., and Wool, M. R. “Aerotherm Charring Material Thermal Response and Ablation Program, Version 3. Volume 1. Program Description and Sample Problems.” 1970.
- [23] Chen, Y. K., and Milos, F. S. “Ablation and Thermal Response Program for Spacecraft Heatshield Analysis.” *Journal of Spacecraft and Rockets*, Vol. 36, No. 3, 1999, pp. 475–483.
- [24] Chen, Y. K., and Milos, F. S. “Two–Dimensional Implicit Thermal Response and Ablation Program for Charring Materials.” *Journal of Spacecraft and Rockets*, Vol. 38, No. 4, 2001, pp. 473–481.
<https://doi.org/10.2514/2.3724>.
- [25] Chen, Y. K., and Milos, F. S. “Multidimensional Finite Volume Fully Implicit Ablation and Thermal Response Code.” *Journal of Spacecraft and Rockets*, Vol. 55, No. 4, 2018, pp. 914–927.
<https://doi.org/10.2514/1.A34184>.
- [26] Wang, Y., Risch, T. K., and Koo, J. H. “Assessment of a One–Dimensional Finite Element Charring Ablation Material Response Model for Phenolic–Impregnated Carbon Ablator.” *Aerospace Science and Technology*, Vol. 91, 2019, pp. 301–309.
<https://doi.org/10.1016/j.ast.2019.05.039>.
- [27] Lachaud, J., and Mansour, N. N. “Porous–Material Analysis Toolbox

- Based on Openfoam and Applications.” *Journal of Thermophysics and Heat Transfer*, Vol. 28, No. 2, 2014, pp. 191–202.
<https://doi.org/10.2514/1.T4262>.
- [28] Dec, J. A. “Three Dimensional Finite Element Ablative Thermal Response Analysis Applied to Heatshield Penetration Design.” *PhD Thesis*, No. May, 2010.
- [29] Dec, J. A., and Braun, R. D. “Three–Dimensional Finite Element Ablative Thermal Response and Design of Thermal Protection Systems.” *Journal of Spacecraft and Rockets*, Vol. 50, No. 4, 2013, pp. 725–734. <https://doi.org/10.2514/1.A32313>.
- [30] Dec, J. A., Braun, R. D., and Laub, B. “Ablative Thermal Response Analysis Using the Finite Element Method.” *Journal of Thermophysics and Heat Transfer*, Vol. 26, No. 2, 2012, pp. 201–212. <https://doi.org/10.2514/1.T3694>.
- [31] Risch, T. K. “Verification of a Finite Element Model for Pyrolyzing Ablative Materials.” *47th AIAA Thermophysics Conference, 2017*, No. June, 2017, pp. 1–35. <https://doi.org/10.2514/6.2017-3354>.
- [32] Amar, A. J., Brandon Oliver, A., Kirk, B. S., Salazar, G., and Droba, J. “Overview of the Charring Ablator Response (CHAR) Code.” *46th AIAA Thermophysics Conference*, No. June, 2016. <https://doi.org/10.2514/6.2016-3385>.
- [33] Ewing, M. E., and Pincock, B. “Heat Transfer Modeling of a Charring Material Using Isoconversional Kinetics.” *Heat Transfer Engineering*, Vol. 38, No. 13, 2017, pp. 1189–1197. <https://doi.org/10.1080/01457632.2016.1239939>.
- [34] Wang, Y., Risch, T. K., and Pasilio, C. L. “Modeling of Pyrolyzing Ablation Problem with Abaqus: A One–Dimensional Test Case.” *Journal of Thermophysics and Heat Transfer*, Vol. 32, No. 2, 2018,

- pp. 542–545. <https://doi.org/10.2514/1.T5274>.
- [35] Sun, H., Mumby, S. J., Maple, J. R., and Hagler, A. T. “An Ab Initio CFF93 All–Atom Force Field for Polycarbonates.” *Journal of the American Chemical Society*, Vol. 116, No. 7, 1994, pp. 2978–2987.
- [36] Sun, H., Ren, P., and Fried, J. R. “The COMPASS Force Field: Parameterization and Validation for Phosphazenes.” *Computational and Theoretical Polymer Science*, Vol. 8, Nos. 1–2, 1998, pp. 229–246. [https://doi.org/10.1016/S1089-3156\(98\)00042-7](https://doi.org/10.1016/S1089-3156(98)00042-7).
- [37] Van Duin, A. C. T., Dasgupta, S., Lorant, F., and Goddard, W. A. “ReaxFF: A Reactive Force Field for Hydrocarbons.” *Journal of Physical Chemistry A*, Vol. 105, No. 41, 2001, pp. 9396–9409. <https://doi.org/10.1021/jp004368u>.
- [38] Park, T., Park, C., Jung, J., and Yun, G. J. “Investigation of Silicon Carbide Oxidation Mechanism Using ReaxFF Molecular Dynamics Simulation.” *Journal of Spacecraft and Rockets*, No. 1, 2020, pp. 1–7. <https://doi.org/10.2514/1.a34669>.
- [39] Morrissey, L. S., Handrigan, S. M., Nakhla, S., and Rahnamoun, A. “Erosion of Spacecraft Metals Due to Atomic Oxygen: A Molecular Dynamics Simulation.” *Journal of Spacecraft and Rockets*, Vol. 56, No. 4, 2019, pp. 1231–1236. <https://doi.org/10.2514/1.A34414>.
- [40] Kulkarni, A. D., Truhlar, D. G., Goverapet Srinivasan, S., Van Duin, A. C. T., Norman, P., and Schwartzentruber, T. E. “Oxygen Interactions with Silica Surfaces: Coupled Cluster and Density Functional Investigation and the Development of a New ReaxFF Potential.” *Journal of Physical Chemistry C*, Vol. 117, No. 1, 2013, pp. 258–269. <https://doi.org/10.1021/jp3086649>.
- [41] Srinivasan, S. G., and Van Duin, A. C. T. “Direction Dependent Etching of Diamond Surfaces by Hyperthermal Atomic Oxygen: A

- ReaxFF Based Molecular Dynamics Study.” *Carbon*, Vol. 82, No. C, 2015, pp. 314–326. <https://doi.org/10.1016/j.carbon.2014.10.076>.
- [42] Rahnamoun, A., and Van Duin, A. C. T. “Reactive Molecular Dynamics Simulation on the Disintegration of Kapton, POSS Polyimide, Amorphous Silica, and Teflon during Atomic Oxygen Impact Using the Reaxff Reactive Force–Field Method.” *Journal of Physical Chemistry A*, Vol. 118, No. 15, 2014, pp. 2780–2787. <https://doi.org/10.1021/jp4121029>.
- [43] Goverapet Srinivasan, S., and Van Duin, A. C. T. “Molecular–Dynamics–Based Study of the Collisions of Hyperthermal Atomic Oxygen with Graphene Using the ReaxFF Reactive Force Field.” *Journal of Physical Chemistry A*, Vol. 115, No. 46, 2011, pp. 13269–13280. <https://doi.org/10.1021/jp207179x>.
- [44] Shi, L., Sessim, M., Tonks, M. R., and Phillpot, S. “Modeling Carbon Fiber Oxidation under High Temperature by Reaxff Based Molecular Dynamics Simulation.” *AIAA Scitech 2020 Forum*, Vol. 1 PartF, No. January, 2020, pp. 6–12. <https://doi.org/10.2514/6.2020-0484>.
- [45] Newsome, D. A., Sengupta, D., and Van Duin, A. C. T. “High–Temperature Oxidation of SiC–Based Composite: Rate Constant Calculation from ReaxFF MD Simulations, Part II.” *Journal of Physical Chemistry C*, Vol. 117, No. 10, 2013, pp. 5014–5027. <https://doi.org/10.1021/jp307680t>.
- [46] Newsome, D. A., Sengupta, D., Foroutan, H., Russo, M. F., and Van Duin, A. C. T. “Oxidation of Silicon Carbide by O₂ and H₂O: A ReaxFF Reactive Molecular Dynamics Study, Part I.” *Journal of Physical Chemistry C*, Vol. 116, No. 30, 2012, pp. 16111–16121. <https://doi.org/10.1021/jp306391p>.
- [47] Qi, T., Bauschlicher, C. W., Lawson, J. W., Desai, T. G., and Reed, E.

- J. “Comparison of ReaxFF, DFTB, and DFT for Phenolic Pyrolysis. 1. Molecular Dynamics Simulations.” *Journal of Physical Chemistry A*, Vol. 117, No. 44, 2013, pp. 11115–11125.
<https://doi.org/10.1021/jp4081096>.
- [48] Harpale, A., Sawant, S., Kumar, R., Levin, D., and Chew, H. B. “Ablative Thermal Protection Systems: Pyrolysis Modeling by Scale–Bridging Molecular Dynamics.” *Carbon*, Vol. 130, 2018, pp. 315–324. <https://doi.org/10.1016/j.carbon.2017.12.099>.
- [49] Desai, T. G., Lawson, J. W., and Koblinski, P. “Modeling Initial Stage of Phenolic Pyrolysis: Graphitic Precursor Formation and Interfacial Effects.” *Polymer*, Vol. 52, No. 2, 2011, pp. 577–585.
<https://doi.org/10.1016/j.polymer.2010.11.018>.
- [50] Jiang, D. E., Van Duin, A. C. T., Goddard, W. A., and Dai, S. “Simulating the Initial Stage of Phenolic Resin Carbonization via the ReaxFF Reactive Force Field.” *Journal of Physical Chemistry A*, Vol. 113, No. 25, 2009, pp. 6891–6894.
<https://doi.org/10.1021/jp902986u>.
- [51] Park, C., Jung, J., and Yun, G. J. “A Multiscale Micromorphic Model with Strain Rate Relationship between MD Simulations and Macroscale Experimental Tests and Dynamic Heterogeneity for Glassy Polymers.” *Composites Part B: Engineering*, Vol. 202, No. September, 2020.
<https://doi.org/10.1016/j.compositesb.2020.108439>.
- [52] Ulz, M. H. “Coupling the Finite Element Method and Molecular Dynamics in the Framework of the Heterogeneous Multiscale Method for Quasi–Static Isothermal Problems.” *Journal of the Mechanics and Physics of Solids*, Vol. 74, 2015, pp. 1–18.
<https://doi.org/10.1016/j.jmps.2014.10.002>.

- [53] Lee, Y., and Basaran, C. “A Multiscale Modeling Technique for Bridging Molecular Dynamics with Finite Element Method.” *Journal of Computational Physics*, Vol. 253, 2013, pp. 64–85.
<https://doi.org/10.1016/j.jcp.2013.06.039>.
- [54] Ziemys, A., Kojic, M., Milosevic, M., Kojic, N., Hussain, F., Ferrari, M., and Grattoni, A. “Hierarchical Modeling of Diffusive Transport through Nanochannels by Coupling Molecular Dynamics with Finite Element Method.” *Journal of Computational Physics*, Vol. 230, No. 14, 2011, pp. 5722–5731. <https://doi.org/10.1016/j.jcp.2011.03.054>.
- [55] Mortazavi, B., Benzerara, O., Meyer, H., Bardon, J., and Ahzi, S. “Combined Molecular Dynamics–Finite Element Multiscale Modeling of Thermal Conduction in Graphene Epoxy Nanocomposites.” *Carbon*, Vol. 60, 2013, pp. 356–365.
<https://doi.org/10.1016/j.carbon.2013.04.048>.
- [56] Park, C., Jung, J., and Yun, G. J. “Multiscale Micromorphic Theory Compatible with MD Simulations in Both Time–Scale and Length–Scale.” *International Journal of Plasticity*, Vol. 129, No. September 2019, 2020, pp. 1–16. <https://doi.org/10.1016/j.ijplas.2020.102680>.
- [57] “ABAQUS Usersubroutine Reference Manual.” *ABAQUS 6.14 Documentation*.
- [58] Steve Plimpton. “Fast Parallel Algorithms for Short–Range Molecular Dynamics.” *Journal of Computational Physics*, Vol. 117, 1995, pp. 1–19.
- [59] Goldstein, H. E. “Pyrolysis Kinetics of Nylon 6–6, Phenolic Resin, and Their Composites.” *Journal of Macromolecular Science: Part A – Chemistry*, Vol. 3, No. 4, 1969, pp. 649–673.
<https://doi.org/10.1080/10601326908053834>.
- [60] Eekelen, T. Van, Lachaud, J. R., Martin, A., and Cozmuta, I.

- “ABLATION TEST–CASE SERIES #3.” *Proceedings of the 5th Ablation Workshop, Lexington, Kentucky*, 2012.
- [61] Lee, D., and Kannatey–Asibu, E. “Numerical Analysis of Ultrashort Pulse Laser–Material Interaction Using ABAQUS.” *Journal of Manufacturing Science and Engineering, Transactions of the ASME*, Vol. 131, No. 2, 2009, pp. 0210051–02100515.
<https://doi.org/10.1115/1.3075869>.
- [62] Li, H., Fan, B., Wang, N., Han, X., Feng, Z., and Guo, S. “Thermal Response Study of Carbon Epoxy Laminates Exposed to Fire.” *Polymer Composites*, Vol. 41, No. 11, 2020, pp. 4757–4770.
<https://doi.org/10.1002/pc.25750>.
- [63] Zhang, Z. “Thermo–Mechanical Behavior of Polymer Composites Exposed to Fire.” *PhD Thesis*, 2010.
- [64] Gordon, S., and McBride, B. . “Computer Program for Calculation of Complex Chemical Equilibrium Compositions and Applications.” *NASA Reference Publication*, Vol. 1311, 1996.
- [65] Moyer, C. B., and Rindal, R. A. “An Analysis of the Coupled Chemically Reacting Boundary Layer and Charring Ablator. Part 2– Finite Difference Solution for the in–Depth Response of Charring Materials Considering Surface Chemical and Energy Balances.” *NASA CR–1061*, 1968.
- [66] Song’, Y., and Smith, F. W. “Effects of Low–Pressure Oxidation on the Surface Composition of Single Crystal Silicon Carbide.” *Journal of the American Ceramic Society*, Vol. 88, No. 7, 2005, pp. 1864–1869. <https://doi.org/10.1111/j.1551-2916.2005.00357.x>.
- [67] Roy, J., Chandra, S., Das, S., and Maitra, S. “Oxidation Behaviour of Silicon Carbide – A Review.” *Reviews on Advanced Materials Science*, Vol. 38, No. 1, 2014, pp. 29–39.

- [68] Jones, J. E. “On the Determination of Molecular Fields. —II. From the Equation of State of a Gas.” *Proceedings of the Royal Society of London. Series A, Containing Papers of a Mathematical and Physical Character*, Vol. 106, No. 738, 1924, pp. 463–477.
<https://doi.org/10.1098/rspa.1924.0082>.
- [69] Verlet, L. “Computer ‘Experiments’ on Classical Fluids. I. Thermodynamical Properties of Lennard–Jones Molecules.” *Physical Review*, Vol. 159, No. 1, 1967, pp. 98–103.
<https://doi.org/10.1103/PhysRev.159.98>.
- [70] Cheung, R. Introduction to Silicon Carbide (SiC) Microelectromechanical Systems (MEMS). In *Silicon Carbide Microelectromechanical Systems for Harsh Environments*, 2006, pp. 1–17.
- [71] Kimoto, T., and Cooper, J. A. Appendix C: Major Physical Properties of Common SiC Polytypes. In *Fundamentals of Silicon Carbide Technology*, IEEE, 2014, pp. 521–524.
- [72] BIOVIA Dassault Systèmes. Material Studio.
- [73] Lachaud, J., Laub, B., Martin, A., and Cozmuta, I. “Ablation Workshop Test Case.” *4th Ablation Workshop*, No. March, 2011, pp. 1–3.
- [74] Lachaud, J. R., Martin, A., Eekelen, T. Van, and Cozmuta, I. “ABLATION TEST–CASE SERIES #2.” *Proceedings of the 5th ablation workshop, Lexington, Kentucky*, 2012, pp. 1–9.
- [75] Lachaud, J., and Mansour, N. N. “Porous–Material Analysis Toolbox Based on Openfoam and Applications.” *Journal of Thermophysics and Heat Transfer*, Vol. 28, No. 2, 2014, pp. 191–202.
<https://doi.org/10.2514/1.T4262>.
- [76] Šimonka, V., Hössinger, A., Weinbub, J., and Selberherr, S. “Growth

Rates of Dry Thermal Oxidation of 4H-Silicon Carbide.” *Journal of Applied Physics*, Vol. 120, No. 13, 2016.

<https://doi.org/10.1063/1.4964688>.

- [77] Vickridge, I., Ganem, J., Hoshino, Y., and Trimaille, I. “Growth of SiO₂ on SiC by Dry Thermal Oxidation: Mechanisms.” *Journal of Physics D: Applied Physics*, Vol. 40, No. 20, 2007, pp. 6254–6263.
<https://doi.org/10.1088/0022-3727/40/20/S10>.

- [78] Kumar, S., and Akhtar, J. “Thermal Oxidation of Silicon Carbide (SiC) – Experimentally Observed Facts.” *Silicon Carbide – Materials, Processing and Applications in Electronic Devices*, 2011.
<https://doi.org/10.5772/20465>.

국문초록

열차폐구조물의 삭마 해석을 위한 멀티스케일 시뮬레이션 환경 구축

박 태 훈

협동과정 우주 시스템 전공

서울대학교 대학원

본 논문은 열차폐 구조물 (TPS)의 멀티스케일 삭마 해석을 위한 기초 연구로서 나노와 매크로 각 스케일에서 독립적인 분석을 수행하는 것을 목표로 한다. 유한 요소 해석을 이용한 매크로 스케일의 탄소/폐놀 복합재의 삭마 분석과 나노 스케일의 분자 동역학 시뮬레이션을 이용한 SiC의 산화 분석을 수행한다. 내부 열전도, 열분해, 가스 확산, 표면 열유속 및 침식과 같이 탄소/폐놀 복합재의 삭마에서 발생하는 다양한 현상들을 Fortran으로 작성된 user subroutine을 이용하여 상용 유한 요소 프로그램 ABAQUS에 적용한다. 개발된 코드는 다양한 경계 조건을 가지는 4가지 1차원 케이스에 대해 외부 프로그램 PATO의 결과와 비교하였으며 결과가 일치한다. 기본적인 2차원 상황에서의 적용 또한 수행된다. SiC의 산화는 분자 동역학을 사용하여 나노 단위에서 분석한다. SiC는 독특한 격자 구조로 인해 복잡한 산화 특성을 나타낸다. 본 논문에서는

표면 방향성과 온도의 영향을 분석한다. 7km/s의 산소원자가 다양한 조건에서 SiC 구조에 충돌하는 시뮬레이션을 수행한다. 표면 방향성에 따른 반응성의 차이는 NVE 조건에서 3개의 표면 방향 (100), (110), (111) 구조를 사용한 시뮬레이션을 통해 분석하고, 온도가 산화에 미치는 영향은 5 가지 온도 (600, 900, 1200, 1800 및 2000K)의 NVT 조건에서 시뮬레이션을 통해 분석한다.

Keywords: 열차폐 구조물, 탄소/폐놀 복합재, 실리콘 카바이드, 멀티 스케일 해석, 분자 동역학, 유한요소해석

Student Number: 2019-25121